Diffuse interface immersed boundary method for low Mach number flows with heat transfer in enclosures

Mukesh Kumar (iD), and Ganesh Natarajan

View Online   **Export Citation**   **CrossMark**

ARTICLES YOU MAY BE INTERESTED IN

Mechanism of pressure oscillation in Taylor-Couette-Poiseuille flow with abruptly contracting and expanding annular gap
Physics of Fluids **31**, 075105 (2019); https://doi.org/10.1063/1.5096583

Enhanced electroosmotic flow of Herschel-Bulkley fluid in a channel patterned with periodically arranged slipping surfaces
Physics of Fluids **31**, 072007 (2019); https://doi.org/10.1063/1.5098508

Single diffusive magnetohydrodynamic pressure driven miscible displacement flows in a channel
Physics of Fluids **31**, 082102 (2019); https://doi.org/10.1063/1.5112373

Diffuse interface immersed boundary method for low Mach number flows with heat transfer in enclosures

View Online   Export Citation   CrossMark

Mukesh Kumar[a] (iD) and Ganesh Natarajan[b]

AFFILIATIONS

Department of Mechanical Engineering, Indian Institute of Technology Guwahati, Guwahati, Assam 781039, India

[a]Electronic mail: mukesh.kr@iitg.ac.in
[b]Present address: Department of Mechanical Engineering, IIT Palakkad, Kerala. Electronic addresses: n.ganesh@iitg.ac.in and n.ganesh@iitpkd.ac.in

ABSTRACT

A novel diffuse interface immersed boundary (IB) approach in the finite volume framework is developed for non-Boussinesq flows with heat transfer. These flows are characterized by variable density, large temperature differences, nonzero velocity divergence, and low Mach numbers. The present IB methodology assumes that the solid body immersed in the domain is filled with a "virtual" fluid and constructs a unified momentum equation that is solved everywhere in the domain. The unified momentum equation is obtained as a convex combination of the Navier-Stokes equation and the no-slip boundary condition employing the solid volume fraction. The hydrodynamic pressure (p) that drives the flow is obtained by the solution of a variable density Poisson equation that is constructed by assuming that the velocity field inside the solid always remains solenoidal although the velocity divergence is nonzero in the fluid domain. The unified Poisson equation is also solved everywhere in the domain and has source terms that depend on the solid volume fraction, temperature gradients, and the spatially invariant thermodynamic pressure (P) that vanish in the Boussinesq limit. The thermodynamic pressure in closed domains follows from the principle of global mass conservation and is used to determine the density field everywhere in the domain except inside the solid where the density remains constant. Numerical simulations are carried out for natural and mixed convective flows in enclosures with stationary and moving heated bodies encompassing both Boussinesq and strongly non-Boussinesq flow regimes. The results of these investigations show that the local Nusselt number distribution over the body surface is oscillatory particularly when grid lines are not aligned with the surface of the body. However, the proposed approach can reasonably accurately compute the average heat transfer in both Boussinesq and non-Boussinesq flows. Investigations show that the heat transfer is significantly enhanced in the non-Boussinesq regime as compared to the Boussinesq regime. A comparison of results from the present approach with those obtained using a body-fitted finite volume solver for stationary bodies demonstrates that the proposed IB approach can compute the flow dynamics quite accurately even on Cartesian meshes that do not conform to the geometry. The IB approach presented herein is a generic approach for quasi-incompressible flows and may be applied to other low Mach number flows such as mixing and reacting flows.

I. INTRODUCTION

The use of Boussinesq approximation in fluid flows with heat transfer is widespread and allows the density to be treated as constant except in the buoyancy term in the momentum equation where changes in density are replaced by changes in temperature. The fluid flow however remains incompressible with the velocity satisfying a zero divergence constraint, and the temperature transport is described by an unsteady convection-diffusion equation. In such cases, the conventional numerical approaches to solve incompressible fluid flows can be applied directly except for the need to handle the equation for temperature (or thermal energy) in addition to the momentum equations. There have been several studies on natural convective flows[1,2] where the temperature differences are small in which case the Boussinesq approximation holds good. Usman and co-workers[3–6] have employed the Boussinesq approximation to

study nanofluid flows in the presence of magnetic field with a focus on analyzing the heat transfer rate and flow physics. However, in problems where there are large temperature gradients, the Boussinesq approximation is inaccurate and can lead to solutions that are not physically meaningful. This is indeed the case in applications such as electronic cooling and industrial furnaces where radiative heat transfer would also play a dominant role. Importantly, the invalidity of the Boussinesq approximation means that the velocity field is no longer solenoidal and hence these flows are also referred to as quasi-incompressible flows. These flows are characterized by low Mach numbers similar to incompressible flows but have a nonzero velocity divergence akin to compressible flows. The governing equations for these non-Boussinesq flows can therefore be derived from the Navier-Stokes equations using a low Mach number formulation[7–9] leading to a set of conservation laws where one can distinguish the hydrodynamic pressure from the thermodynamic pressure. The thermodynamic pressure is defined by the equation of state (EOS) and remains spatially invariant in low Mach number flows, while the hydrodynamic pressure which does not have an evolution equation is responsible for driving the flow. Evidently, numerical methods to solve quasi-incompressible flows need to account for the presence of "twin" pressures and the nonzero velocity divergence, and there have been relatively fewer efforts to study low Mach number flows with heat transfer in the open literature.

The earliest numerical studies in non-Boussinesq convection are due to Quéré et al.[10] using pseudospectral approaches. There have been subsequent efforts using finite volume[11] and finite element approaches[12] to handle large temperature difference thermobuoyant flows. While the work of Dick and Vierendeels[11] employed the density-based solver with low Mach number preconditioning, the investigations of Darbandi and co-workers extended the pressure-based SIMPLE approach to solve non-Boussinesq natural convective flows. There have also been recent efforts employing the low Mach formulation for laminar convective-radiative heat transfer problems on unstructured meshes[13] as well as turbulent high temperature convection on structured grids.[14] The low Mach number approach has also been widely employed to study reacting flows by many authors.[15] All these studies in non-Boussinesq heat transfer have employed conventional body-fitted meshes in conjunction with staggered or collocated grid frameworks to solve the conservation laws. However, in problems wherein the geometry could be complex (such as in electronic packaging) and in scenarios requiring studies on several designs (for instance, in building energy simulations[16]), the use of conformal meshes demand user expertise in mesh generation and the need to regenerate meshes for similar-looking geometries would add to computational cost.

The emergence of Cartesian immersed boundary (IB) frameworks has been motivated by the need to have a simple, easy, and automated mesh generation process. A good overview of these approaches can be found in the work of Mittal and Iaccarino,[17] and IB approaches have been broadly divided as sharp and diffuse interface immersed boundary approaches. The methods that fall in the category of sharp interface IB approaches enforce the boundary conditions directly on the geometric interface and include, among others, the ghost cell IB method[18] and Hybrid Cartesian IB method[19] which have been extensively used in problems ranging from aquatic locomotion to compressible flows. The diffuse interface IB methods constitute all techniques that do not preserve the interface of

the geometry sharp and a large class of techniques such as the fictitious domain method,[20] Brinkman penalization approach,[21,22] and the volume-of-solid immersed boundary method[23] fall in this category. It must be pointed out that while IB approaches have been extensively used for incompressible fluid flows, there have been a lesser number of studies that have tackled flows with heat transfer. The studies in Refs. 24–27 have all employed different class of IB techniques for Boussinesq heat transfer. Wang et al.[24] have proposed a boundary condition enforced immersed boundary lattice Boltzmann flux solver, while De[27] has proposed a diffuse interface IB approach to simulate fluid flows with heat transfer in the Boussinesq limit. The only known efforts, to the best of authors' knowledge, that have employed IB approaches in low Mach flows are the studies targeted at understanding human phonation and flow induced noise,[28] those on turbulent multiphase and reacting flows[29] and studies for fully resolved reacting gas-particulate flows.[30] While the latter work employed the fictitious domain approach, the other studies employed a sharp interface IB methodology with only one of these three studies accounting for heat transfer as well. The choice of sharp interface IB methods is owing to their ability to sharply represent the geometric interface, but recent studies[27,31] have shown that diffuse IB approaches, despite diffusing the interface over a few cell widths, perform equally well as the sharp interface counterparts. Moreover, sharp interface IB methods are not free of issues and the problem of spurious force oscillations (SFOs) in simulations with moving boundaries is well-documented.[32] Investigations in Ref. 31 have shown that diffuse interface approaches can dampen out SFOs without unduly affecting the solution accuracy. A very recent study using sharp interface IB approaches[33] has also found that the lack of discrete energy conservation, inherent to this class of methods, is responsible for underprediction of heat flux in hypersonic laminar flows.

The lack of studies involving non-Boussinesq heat transfer in closed domains which can have practical applications in electronic cooling and building design motivates the present study. We choose to pursue the diffuse interface IB approach in Ref. 23 since these have been shown to perform as well as sharp-interface IB methods, exhibit lesser SFOs, and are discretely conservative. The simplicity and ease of implementation of the approach in existing finite volume frameworks are added advantages as well. It must be remarked that the development and implementation of the diffuse interface IB method for quasi-incompressible flows in enclosures is a nontrivial proposition. While the thermodynamic pressure has no role to play in genuinely incompressible flows, it is dictated by the equation of state (EOS) and remains always constant in low Mach number flows in open domains (such as those in combustion). However, for thermobuoyant flows in enclosures, the thermodynamic pressure is only spatially constant and its time derivative influences the energy equation as well as the calculation of hydrodynamic pressure which in turn drives the flow. The coupling between the thermodynamic and hydrodynamic pressure in the evolution equation for the latter therefore needs to be accounted properly in the diffuse interface IB framework, and there have been no studies that have explored this aspect until date. The novelty of present work may be summarized as follows.

- The development of a volume-of-solid based diffuse interface IB method to compute non-Boussinesq flows in natural

and mixed convection regimes and to assess its performance in computing the flow and thermal patterns as well as heat transfer.

- Low Mach number finite volume (FV) solver is combined with a diffuse interface immersed boundary approach to devise a novel IB-FV solver for non-Boussinesq flows where "unified" equations are solved in the entire computational domain for momentum and energy conservation.
- Generalizes the IB approach to handle variable density quasi-incompressible flows and highlight the strengths and weaknesses of the IB-FV solver by carrying out detailed investigations of free and mixed convective heat transfer problems.
- Proposed methodology provides a single framework to solve Boussinesq and non-Boussinesq flows and a pathway to devise such approaches for fully compressible flow.

The remainder of the manuscript is organized as follows. Sections II and III discuss the low Mach number formulation and the finite volume discretization of the governing equations, respectively. The diffuse interface IB approach is discussed in detail with specific emphasis on its implementation for generic low Mach flows with heat transfer in Sec. IV. A number of test cases including stationary and moving geometries, both in the Boussinesq and non-Boussinesq regimes, are described in Sec. V. Some discussions on the viability and versatility of the proposed IB approach and directions for future research constitute Sec. VI.

II. LOW MACH NUMBER FORMULATION

The governing equations for genuinely compressible fluid flows with constant thermophysical properties are the Navier-Stokes equations. The conservation laws[34] for mass, momentum, and energy read

$$\frac{\partial \rho}{\partial t} + \nabla \cdot (\rho \mathbf{u}) = 0, \tag{1}$$

$$\frac{\partial (\rho \mathbf{u})}{\partial t} + \nabla \cdot (\rho \mathbf{u}\mathbf{u}) = -\nabla p + \nabla \cdot \bar{\bar{\tau}} + (\rho_\infty - \rho)g\hat{\mathbf{e}}_y, \tag{2}$$

$$\frac{\partial (\rho \theta)}{\partial t} + \nabla \cdot (\rho \theta \mathbf{u}) = \frac{k}{C_p}\nabla^2 \theta + \frac{1}{C_p}\frac{Dp}{Dt} + \frac{1}{C_p}\bar{\bar{\tau}}:\nabla\mathbf{u}, \tag{3}$$

where

$$\bar{\bar{\tau}} = \mu\Big(\nabla\mathbf{u} + (\nabla\mathbf{u})^T - \frac{2}{3}(\nabla\cdot\mathbf{u})\mathbf{I}\Big).$$

The ideal gas equation of state is assumed in this study

$$p = \rho R\theta. \tag{4}$$

The nondimensionalization of these equations is carried out by choosing speed of sound (C_o) as the velocity scale, while the scales for pressure and density are the initial thermodynamic pressure and density inside the enclosure. The temperature reference scale is chosen as the mean temperature of the enclosure, while the reference time scale is $\frac{L}{U}$, where L is the characteristic length scale, γ is the ratio of specific heats, and U is the characteristic fluid velocity. The dimensionless conservative laws are given by

$$\frac{\partial \rho}{\partial t} + \frac{1}{Ma}\nabla \cdot (\rho \mathbf{u}) = 0, \tag{5}$$

$$\frac{\partial (\rho \mathbf{u})}{\partial t} + \frac{1}{Ma}\nabla \cdot (\rho \mathbf{u}\mathbf{u}) = -\frac{1}{\gamma Ma}\nabla p + \frac{1}{Re}\nabla \cdot \bar{\bar{\tau}} + \frac{Ma}{Fr}(\rho_\infty - \rho)g\hat{\mathbf{e}}_y, \tag{6}$$

$$\frac{\partial (\rho \theta)}{\partial t} + \frac{1}{Ma}\nabla \cdot (\rho \theta \mathbf{u}) = \frac{k}{C_p}\Bigg\{\frac{1}{RePr}\nabla^2\theta + \frac{\gamma-1}{\gamma}\Big(\frac{\partial \rho}{\partial t} + \frac{1}{Ma}\mathbf{u}\cdot\nabla p\Big)$$
$$+ \frac{\gamma-1}{Re}\bar{\bar{\tau}}:\nabla\mathbf{u}\Bigg\}, \tag{7}$$

where the nondimensional numbers appearing in the equations are the Froude number Fr, Mach number Ma, Prandtl number Pr, and Reynolds number Re and are defined as

$$Fr = \frac{U^2}{g_o L}, \quad Ma = \frac{U}{C_o}, \quad Pr = \frac{\nu}{\alpha}, \quad \gamma = \frac{C_p}{C_v}, \quad Re = \frac{U_\infty L}{\nu}.$$

The low Mach number flows with heat transfer discussed in this work are referred to as quasi-incompressible and are characterized by Mach numbers of 10^{-3} or lesser. One can arrive at the low Mach number equations[35] by expanding the velocities as well as thermodynamic variables in a small parameter Ma as follows:

$$\mathbf{u} = Ma\Big[\mathbf{u}^{(0)} + Ma^2\mathbf{u}^{(1)} + o(Ma^2)\Big], \tag{8}$$

$$\theta = \theta^{(0)} + Ma^2\theta^{(1)} + o(Ma^2), \tag{9}$$

$$p = P^{(0)} + Ma^2 p^{(1)} + o(Ma^2), \tag{10}$$

$$\rho = \rho^{(0)} + Ma^2\rho^{(1)} + o(Ma^2). \tag{11}$$

One can see that $P^{(0)}$ appearing in the asymptotic expansion for pressure is essentially the background pressure which is also referred to as the thermodynamic pressure. The second order perturbation $p^{(1)}$ appearing in the asymptotic expansion represents the hydrodynamic pressure, and its gradient drives the flow. We denote the thermodynamic and hydrodynamic pressure as P and p, respectively, and the superscripts are dropped for sake of convenience. The low Mach number equations may be obtained by comparing terms of $O(1)$ and $O(Ma^2)$, and one may refer to work of Paolucci[35] for the details of these equations. The dimensional form of the low Mach number equations is given as follows:

$$\frac{\partial \rho}{\partial t} + \nabla \cdot (\rho \mathbf{u}) = 0, \tag{12}$$

$$\frac{\partial (\rho \mathbf{u})}{\partial t} + \nabla \cdot (\rho \mathbf{u}\mathbf{u}) = -\nabla p + \nabla \cdot \bar{\bar{\tau}} + (1-\rho)\hat{\mathbf{e}}_y, \tag{13}$$

$$\frac{\partial (\rho \theta)}{\partial t} + \nabla \cdot (\rho \mathbf{u}\theta) = \frac{k}{C_p}\nabla^2\theta + \frac{1}{C_p}\Big(\frac{dP}{dt}\Big), \tag{14}$$

$$P = \rho r\theta. \tag{15}$$

One can clearly see that the low Mach number equations have two distinct pressure fields, the hydrodynamic pressure $p(x, t)$ and the thermodynamic pressure $P(t)$. It must be remarked that the latter depends on the equation of state (EOS) and is only a function of time. The thermodynamic pressure thus remains constant (at any given time instant) everywhere in space, while the hydrodynamic

pressure varies both in space and time. We consider the nondimensionalization of the low Mach conservation laws by choosing suitable reference scales. The velocity scale is chosen as $\sqrt{g\beta L\Delta\theta}$ for natural convection flows, while it is U_∞ (which is imposed) for mixed convection flows. The temperature is nondimensionalized as $\theta^* = \frac{\theta-\theta_o}{\theta_h-\theta_c}$, where θ_h and θ_c are the temperatures of hot and cold walls and θ_o is a simple average of these values. The hydrodynamic pressure is nondimensionalized, akin to incompressible flows as, $p^* = \frac{p-P_o}{\rho_\infty U_\infty^2}$, where P_o is the reference scale for thermodynamic pressure and the velocity scale is different for free and mixed convection flows. The dimensionless time scale is $\frac{L}{U_\infty}$. The final system of dimensionless conservation laws in the low Mach number limit (dropping * for convenience) is

$$\frac{\partial \rho}{\partial t} + \nabla \cdot (\rho \mathbf{u}) = 0, \tag{16}$$

$$\frac{\partial(\rho\mathbf{u})}{\partial t} + \nabla \cdot (\rho\mathbf{uu}) = -\nabla p + C_1(\nabla \cdot \bar{\bar{\tau}}) + C_2(1-\rho)\hat{\mathbf{e}}_\mathbf{y}, \tag{17}$$

$$\frac{\partial(\rho\theta)}{\partial t} + \nabla \cdot (\rho\mathbf{u}\theta) = C_3\nabla^2\theta + C_4\left(\frac{dP}{dt}\right), \tag{18}$$

$$P = (1 + Ga\theta)\rho, \tag{19}$$

where the dimensionless numbers appearing in coefficients C_1, C_2, C_3, and C_4 (shown in Table I) include the Rayleigh number Ra, the Richardson number Ri, and the Gay–Lussac number Ga which are defined as

$$Ga = \beta(\theta_h - \theta_c), \quad Ra = \frac{g\beta L^3(\theta_h-\theta_c)}{\alpha\nu}, \quad Ri = \frac{Ra}{PrRe^2}.$$

We assume that the fluid has constant viscosity and thermal conductivity in our studies although a generalization for variable fluid/thermal properties is a relatively straightforward affair. An important aspect of the numerical solution to the low Mach conservation laws is the computation of thermodynamic (P) and hydrodynamic pressures. The latter which drives the flow does not have a natural evolution equation, and we defer its discussion to Sec. IV. The thermodynamic pressure P is constant in both space and time for open systems, but for closed systems considered in this work, the thermodynamic pressure is only spatially invariant and we obtain an expression for the time dependent thermodynamic pressure from the principle of global mass conservation. Realizing that the total mass of a closed system remains invariant with time, we have

$$P = \frac{m^0 + Ga\int_{\Omega_d}(\rho\theta)d\Omega}{\int_{\Omega_d} d\Omega}, \tag{20}$$

TABLE I. The nondimensional coefficients of governing equations.

	C_1	C_2	C_3	C_4
Natural convection	$\sqrt{\frac{Pr}{Ra}}$	$\frac{1}{Ga}$	$\sqrt{\frac{1}{PrRa}}$	$\frac{\gamma-1}{\gamma Ga}$
Mixed convection	$\frac{1}{Re}$	$\frac{Ri}{Ga}$	$\frac{1}{RePr}$	$\frac{\gamma-1}{\gamma Ga}$

where m^0 is the initial mass in the enclosure and Ω_d is the total volume of the enclosure. The velocity field in quasi-incompressible flows is nondivergent, and an expression for velocity divergence can be easily derived. Rearranging the thermal energy equation Eq. (18) and employing the continuity equation gives

$$\nabla \cdot \mathbf{u} = \frac{1}{P}\left[C_3 Ga\nabla^2\theta - \frac{1}{\gamma}\frac{dP}{dt}\right]. \tag{21}$$

Realizing that $\frac{dP}{dt}$ is constant everywhere in the domain and that all boundaries are impermeable leads to

$$\frac{dP}{dt} = \gamma\frac{C_3 Ga}{\Omega_d}\int_{\delta\Omega_d}\nabla^2\theta\, d\Omega, \tag{22}$$

where $\delta\Omega_d$ is the boundary of the computational domain Ω_d that is occupied by fluid. It is easy to see that in the Boussinesq limit, $Ga \to 0$, and we recover the zero velocity divergence constraint. Consequently, the thermodynamic pressure P becomes spatially and temporally invariant. The low Mach formulation therefore encompasses genuinely incompressible flows and allows for a unified treatment of Boussinesq and non-Boussinesq flows with a single algorithm.

III. HYBRID STAGGERED/NONSTAGGERED FINITE VOLUME APPROACH

We briefly describe in this section finite volume discretization of the low Mach number equations presented in Sec. II. We employ a novel hybrid staggered/nonstaggered framework as also described in Ref. 7 to solve the conservative laws. The key idea of the proposed framework is that we solve the scalar momentum equation at the cell faces as opposed to the collocated framework. Therefore, independent of the dimensionality of the problem, we solve a single scalar equation for the normal momentum equation which is obtained by projecting the momentum equation (17) along the normal direction to the face (see Fig. 1). Employing a fractional-step approach akin to incompressible flows leads to the following discrete equation for normal momentum:

$$\frac{3(\rho U)_f^* - 4(\rho U)_f^m + (\rho U)_f^{m-1}}{2\Delta t} = -\frac{1}{\Omega}\mathbb{C}(U_f^*, \mathbf{u}^*) - \frac{\delta p^m}{\delta n}\Big|_f$$
$$+ \frac{1}{\Omega}C_1\mathbb{D}(U_f^*, \mathbf{u}^*) + C_2(1-\rho_f^m)n_{y,f}, \tag{23}$$

where

$$\mathbb{C}(U_f^*, \mathbf{u}^*) = \left[\sum_{e\in E(\Omega)}\rho_e\mathbf{u}_e^* U_e^*\Delta S_e\right]\cdot\mathbf{n}_f,$$

$$\mathbb{D}(U_f^*, \mathbf{u}^*) = \left[\sum_{e\in E(\Omega)}\left(\nabla\mathbf{u}_e + (\nabla\mathbf{u}_e)^T - \frac{2}{3}(\nabla\cdot\mathbf{u})\mathbf{I}\right)\cdot\mathbf{n}_e\,\Delta S_e\right]\cdot\mathbf{n}_f,$$

where ΔS_e and $\mathbf{n}_e$ refer to the surface area and outward unit normal of the edge "e", respectively. It must be remarked that Ω represents the union of two cells sharing the face "f," where the normal
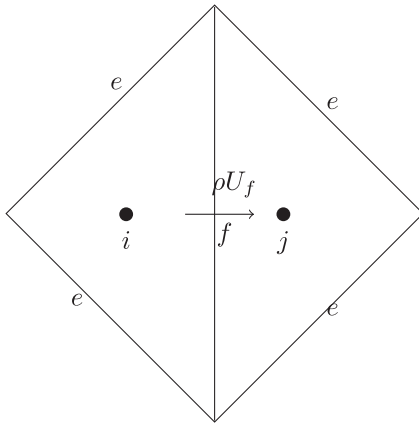
FIG. 1. The control volume for normal momentum combines the two adjacent cells i and j ($\Omega = \Omega_i \cup \Omega_j$).

momentum ρU_f is computed and the "*" denotes the auxiliary or provisional momentum values which are subsequently corrected. Although the solution to the momentum at the faces is similar to staggered mesh approaches, the convective and diffusive fluxes appearing in Eq. (23) are calculated in the same manner as in a non-staggered framework. Therefore, the viscous fluxes computed using central differencing while the convective fluxes are calculated using a second-order bounded upwind-biased scheme with the hydrodynamic pressure appear as a normal derivative in the momentum equation. It must be noted that the summation in Eq. (23) is over all faces of the combined control volume Ω. The energy equation that defines the temperature field (which is scalar) is solved at the cell center (see Fig. 2) like in a collocated framework. The treatment of convective and diffusive fluxes for the energy equation is similar to those for momentum described previously and the discrete energy equation reads
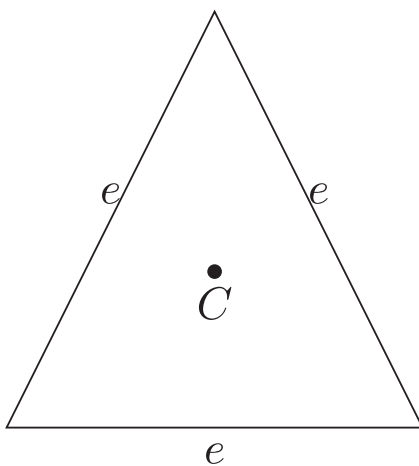

FIG. 2. The control volume (Ω_c) for solution of scalar variables like energy ($\rho\theta$) and pressure correction (Φ).

$$\Omega_c \frac{3(\rho\theta)_c^{m+1} - 4(\rho\theta)_c^m + (\rho\theta)_c^{m-1}}{2\Delta t} + \sum_{e\in E(\Omega_c)} (\rho\theta)_e^{m+1} U_e^{m+1} \Delta S_e$$
$$= C_3 \sum_{e\in E(\Omega_c)} \frac{\delta\theta}{\delta n}\Big|_e^{m+1} \Delta S_e + C_4 \frac{dP^{m+1}}{dt} \Omega_c, \qquad (24)$$

where Ω_c is the volume of the cell at which the temperature is computed and the summation is over all the faces of this cell. It must be realized that the temperature discretization is also second-order accurate and employs three-point backward differencing (BDF2) which needs to be "started" using first-order Euler time stepping. This however does not affect the overall second-order temporal accuracy of the solver. The construction of the discrete equation for the evolution of hydrodynamic pressure "p" is a critical aspect of the solution procedure. The hydrodynamic pressure drives the flow but does not have a natural evolution equation. Following the fractional step approach, we subtract the normal momentum equations at "*" and $(m + 1)$-th time levels which gives

$$\frac{U_f^{m+1} - U_f^*}{\Delta t} = -\frac{2}{3\rho^{m+1}} \frac{\delta\Phi}{\delta n}\Big|_f, \qquad (25)$$

where $\Phi = p^{m+1} - p^m$ is the correction to hydrodynamic pressure. It must be remarked that Eq. (25) is only an approximation since the differences of the convective and diffusive flux contributions have been neglected which introduces second-order errors. Summing up Eq. (25) overall faces of a cell gives

$$\frac{2}{3}\Delta t \sum_{e\in E(\Omega_c)} \frac{1}{\rho_e^{m+1}} \frac{\delta\Phi}{\delta n}\Big|_e \Delta S_e = - \sum_{e\in E(\Omega_c)} U_e^{m+1} \Delta S_e + \sum_{e\in E(\Omega_c)} U_e^* \Delta S_e, \qquad (26)$$

which may be interpreted as the discrete Poisson equation for hydrodynamic pressure correction. It must be realized that $\sum_{e\in E(\Omega_c)} U_e^{m+1} \Delta S_e$ represents the discrete divergence constraint at $(m + 1)$-th time level which follows from Eq. (21) as

$$\sum_{e\in E(\Omega_c)} U_e^{m+1} \Delta S_e = \frac{1}{P}\left[C_3 Ga \sum_{e\in E(\Omega_c)} \frac{\delta\theta}{\delta n}\Big|_e \Delta S_e - C_4 \frac{dP}{dt}\Omega_c \right]. \qquad (27)$$

One can clearly see that as $Ga \to 0$, the incompressibility constraint is recovered. The normal derivative for "p" (in the momentum equation) and Φ (in the Poisson equation) is obtained using standard central differencing which for the pressure correction reads

$$\frac{\delta\Phi}{\delta n}\Big|_f \approx \frac{\Phi_j - \Phi_i}{\Delta n}, \qquad (28)$$

where the subscripts j and i refer to the centroids of cells sharing the face f and Δn refers to the distance between centroids of i and j cells. It must be realized that unlike the hydrodynamic pressure, the thermodynamic pressure P is defined by EOS. Importantly, P remains constant everywhere in a closed domain for any given time instant. The value of P^{m+1} follows from the discrete analog of Eq. (20) and reads

$$P^{m+1} = \frac{m^o + Ga \sum (\rho\theta)_c^{m+1}\Omega_c}{\sum \Omega_c}, \qquad (29)$$

where $m^0 = \sum \rho_c^{(0)}\Omega_c$ is the total initial mass in the enclosure and the summation in Eq. (29) is over all cells. We stress that the solution

approach also requires the time derivative of thermodynamic pressure $\frac{dP}{dt}$ which appears as a source term, both in the Poisson equation Eq. (26) as well as the energy Eq. (24). This may be determined from a discrete analog of Eq. (22) as

$$\frac{dP}{dt} = \frac{\gamma}{\Omega_d} C_3 Ga \sum_{e \in (\delta\Omega_d)} \frac{\delta\theta}{\delta n}\Big|_e \Delta s_e. \tag{30}$$

The discretization of the normal derivative of θ is similar to that of Φ and p and employs central differencing. We must remark herein that the quantity $\frac{dP}{dt}$ is treated implicitly in the solution of energy equation which leads to a more robust solution approach particularly for large values of Ga. The computation of density follows from EOS as

$$\rho^{m+1} = P^{m+1} - Ga(\rho\theta)^{m+1}, \tag{31}$$

where the quantities in the RHS of Eq. (31) are obtained from the discrete global mass preservation condition Eq. (29) and the solution to the energy equation Eq. (24). The normal momentum and hydrodynamic pressure at $(m+1)$-th time level are obtained through a correction step that reads

$$p^{m+1} = p^m + \Phi, \quad (\rho U)_f^{m+1} = (\rho U)_f^* - \frac{2}{3}\Delta t \frac{\delta\Phi}{\delta n}\Big|_f. \tag{32}$$

The centroidal velocities u^{m+1} and v^{m+1} are recovered through a vector interpolation strategy[36] and are given by

$$\mathbf{u}_c^{m+1} = \frac{1}{\Omega_c} \sum_{e \in E(\Omega_c)} U_e^{m+1}(\mathbf{x}_f - \mathbf{x}_c)\Delta S_e, \tag{33}$$

where $\mathbf{x}_f$ and $\mathbf{x}_c$ are the position vector of face and cell center, respectively, while Ω_c represents the cell volume. Summarizing the strategy, we stress that while the normal momentum equation is solved for at the faces as in a staggered framework, the energy and Poisson equations are solved at the cell centers like in a collocated framework. This unique hybrid staggered/nonstaggered framework has been previously employed for incompressible flows where its accuracy and conservation properties have been studied.[37,38] We also remark that the implicit nonlinear equation for normal momentum is solved using the Newton-Krylov solver with help of PetSc libraries,[39] while the linear systems of equations arising from the discrete equations for energy and hydrodynamic pressure correction are solved using GMRES/BiCGSTAB solvers with SAAMG preconditioning implemented using LiS libraries.[40] A summary of the numerical methodology (see Algorithm 1) pertaining to the FV framework in the present study is presented below.

We can consider the genuinely incompressible flows as a limiting case of quasi-incompressible flows discussed here when $Ga \to 0$. In this limit, the thermodynamic pressure becomes constant both in space and time [see Eq. (29)] and its temporal derivative in Eq. (30) vanishes identically. As a result, the discrete divergence condition in Eq. (27) reduces to the familiar constraint of a solenoidal velocity field and the thermal energy equation Eq. (24) is devoid of the source term that otherwise needs an implicit treatment. The low Mach number finite volume solver is therefore a generalization that considers a nonsolenoidal velocity divergence, and the presence of a time-dependent pressure for large values of Ga along with a variable density field makes the treatment of the energy and Poisson equations different from those for standard incompressible solvers. These

ALGORITHM 1. Solution methodology of hybrid staggered/nonstaggered framework.

1. Initialize all conserved and primitive quantities in the domain.
2. Solve the energy equation Eq. (24) for temperature (θ^{m+1}) using ρ^m.
3. Determine thermodynamic pressure (P^{m+1}) using Eq. (29).
4. Calculate density (ρ^{m+1}) from θ^{m+1} and P^{m+1}, using Eq. (31).
5. Solve the scalar normal momentum equation $[(\rho U)_f^*]$ using Eq. (23).
6. Solve the pressure correction equation (Φ) using Eq. (26).
7. Obtain the $(\rho U)_f^{m+1}$ and P^{m+1} from Eq. (32).
8. Obtain the centroidal velocities (u^{m+1}, v^{m+1}) from Eq. (33).
9. Go to step 2 and reiterate the process until convergence criterion is satisfied.

complexities also pose challenges when devising the diffuse interface immersed boundary method which is described in greater detail in Sec. IV.

IV. DIFFUSE INTERFACE IMMERSED BOUNDARY METHOD

This section is devoted to the description of the diffuse interface immersed boundary (IB) method in the hybrid staggered/nonstaggered finite volume framework discussed in Sec. III. The diffuse interface IB methodology is based on the work of Pan[23] which employs an indicator function to construct a "unified" equation that is solved everywhere in the domain. This approach has been previously extended for solving flows with heat transfer[27] as well as multiphase flows[31] in the incompressible flow regime. We attempt to exploit the diffuse interface IB approach to construct a unique IB-FV framework that is capable of solving both Boussinesq and non-Boussinesq flows, thereby extending the approach to handle quasi-incompressible flows. We now highlight the major differences between the proposed IB-FV solver and its incompressible counterparts[23,27,31] to highlight the challenges for the development of such a framework.

1. All previous studies that employ the volume-of-solid approach[23,27,31] have dealt with incompressible flows. De[27] considered single phase flows, while the diffuse interface IB approach was employed for multiphase flows in the investigations of Patel and Natarajan.[31] However, low Mach number flows discussed in this work are quasi-incompressible which means that the zero velocity divergence constraint no longer holds good.

2. Previous studies[27,31] have considered a single pressure field for hydrodynamic pressure only. Low Mach number flows have two distinct pressure fields which must be accounted for by the numerical framework. Specifically, for flows in enclosures, the thermodynamic pressure is spatially constant but temporally varying, in general.

3. Non-Boussinesq flows studied herein are variable density single phase flows. Earlier investigations[23] have considered constant density single phase flows and two-phase flows[31] where the density of each phase is necessarily constant.
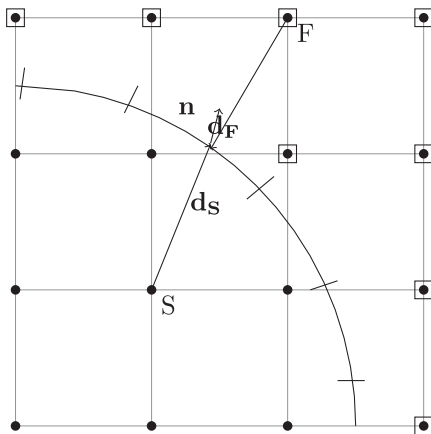
FIG. 3. Schematic of the node classification algorithm.

These salient differences show that the construction of a diffuse interface IB-FV solver for low Mach numbers is a nontrivial proposition. Nevertheless, the basic philosophy behind such a framework remains unaltered—to treat the solid analogous to the fluid so that "unified" conservation laws may be devised. These "unified" governing equations are dependent on the solid volume fraction (also referred to as solid fraction) and are constructed to satisfy the Navier-Stokes equations in the fluid regions and the relevant boundary condition within the solid. We elucidate the computation of the solid fraction ϕ_B (Sec. IV A) and the construction of the unified governing equation in Sec. IV B.

A. Computation of solid fraction

The solid fraction ϕ_B is an indicator function that denotes the fraction of solid occupying a given cell. The body is assumed to be composed of a finite number of Lagrangian marker points and is then "immersed" into the underlying Cartesian mesh. We first identify the nodes inside the body (solid nodes denoted S) and outside of it (fluid nodes denoted F), as shown in Fig. 3. The node classification algorithm is summarized (see Algorithm 2).

The node classification algorithm is applied only to nodes inside a "bounding box"[41] containing the solid body. All nodes outside of the box are fluid nodes, and this reduces the total cost the classification algorithm. Furthermore, the nearest face is also determined in a computationally efficient manner as also described in

---

ALGORITHM 2. Node classification.

---

1. For each node, we identify the nearest face on the body.
2. Calculate the vector $\mathbf{d} = \mathbf{x}_{nf} - \mathbf{x}$, where $\mathbf{x}$ and $\mathbf{x}_{nf}$ are the position vectors of the node and the centroid of the nearest face, respectively.
3. Evaluate the scalar product $\mathbf{d} \cdot \mathbf{n}_{nf}$ where $\mathbf{n}_{nf}$ is the unit outward normal to the face.
4. If the scalar product is positive, then the node is a solid node, else it is a fluid node.

ALGORITHM 3. Solid fraction computation.

---

1. Divide every "I" cell into a "virtual" $N \times N$ sub-grid consisting of N^2 sub-cells.
2. Apply the "node classification" algorithm to the cell-centers of those sub-cells. Let the number of sub-cells classified as being solid be equal to N_v.
3. The solid fraction of the cell is $\phi_B = \frac{N_v}{N^2}$.

Ref. 42. It is now possible to classify all the cells in the mesh into three categories. A cell for which all nodes are solid nodes is a solid cell ("S"). The fluid cells ("F") are those for which all nodes are fluid nodes. All cells that do not fall in these two categories are the immersed ("I") cells. One can easily recognize that "I" cells are those cells that necessarily contain some part of the solid geometry and therefore $0 < \phi_B < 1$ in these cells. By definition, $\phi_B = 1$ in "S" cells and $\phi_B = 0$ in "F" cells. The algorithm to obtain the true volume fraction each "I" cell is described (see Algorithm 3).

The algorithm is a simple reuse of the node classification approach to virtual subcells and gives a reasonable accurate estimate of the solid fraction if sufficient number of subcells are considered. In studies herein, we use $N = 5$ or 6 (which corresponds to 25 or 36 subcells per "I" cell). Figure 4 shows an illustration of this approach which has been found to be quite accurate in computing the solid fraction in the test cases discussed herein.

B. Unified momentum and energy equation

The key principle behind the diffuse interface IB approach is to solve "unified" conservation laws everywhere in the domain. The "unified" equations must satisfy the following conditions.

1. It must reduce to the governing equations for the fluid flow in the "F" cells ($\phi_B = 0$).
2. It must reduce to the boundary conditions in the "S" cells ($\phi_B = 1$).
3. It must be a weighted combination of the governing equations and the boundary conditions in the "I" cells ($0 < \phi_B < 1$).
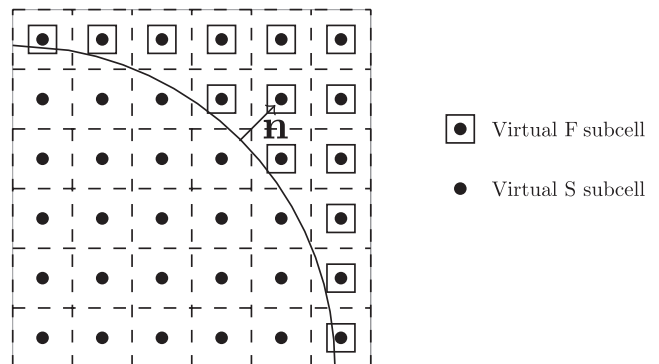

FIG. 4. Illustration of volume fraction computation for "I" cells. In this case, $\phi_B = \frac{22}{36}$.

We consider herein viscous flows with isothermal walls and therefore the unified normal momentum equation reads

$$(1 - \phi_B)\left[\frac{3(\rho U)_f^* - 4(\rho U)_f^m + (\rho U)_f^{m-1}}{2\Delta t} + \frac{1}{\Omega}\mathbb{C}(U_f^*, \mathbf{u}^*) + \left.\frac{\delta p}{\delta n}\right|_f^m \right.$$
$$\left. - \frac{1}{\Omega}\mathbb{D}(U_f^*, \mathbf{u}^*) - C_2(1 - \rho_f^m)n_{y,f} \right] = -\phi_B\left[\frac{\rho U_f^{m+1} - 3(\rho U)_B}{2\Delta t} \right],$$

(34)

where U_B refers to the normal velocity of the body surface that is also imposed within the solid thereby enforcing the no-slip condition. This value is identically zero for stationary bodies while in case of moving bodies may either be imposed to a nonzero value or computed from ancillary equations. In a similar vein, the unified energy equation reads

$$(1 - \phi_B)\left[\Omega_c \frac{3(\rho\theta)_c^{m+1} - 4(\rho\theta)_c^m + (\rho\theta)_c^{m-1}}{2\Delta t} + \sum_{e\in E(\Omega_c)} (\rho\theta)_e^{m+1} U_e^{m+1} \Delta S_e \right.$$
$$\left. - C_3 \sum_{e\in E(\Omega_c)} \left.\frac{\delta\theta}{\delta n}\right|_e^{m+1} \Delta S_e - C_4 \frac{dP^{m+1}}{dt}\Omega_c \right]$$
$$= -\phi_B\left[\frac{3(\rho\theta)_c^{m+1} - 3(\rho\theta)_B}{2\Delta t} \right]\Omega_c,$$

(35)

where θ_B refers to the constant temperature imposed on the surface of the solid. It must be remarked that the "unified" momentum equation can be recast as a nonlinear scalar equation, while the "unified" energy equation leads to a system of linear algebraic equations. The reasoning of a "unified" equation is based on the assumption that the solid is filled with a virtual fluid which allows the solid region to be treated as if it were a fluid, in conjunction with the correct boundary conditions. The single phase flows in Refs. 23 and 27 considered the same fluid both inside and outside the solid, while the "virtual" fluid was the densest (and most viscous) of all fluids in a multiphase context.[31] The choice of the "virtual" fluid for variable density single phase flows considered in this work remains to be addressed and is discussed in Sec. IV C.

C. Choice of virtual fluid

The basic philosophy of the diffuse interface IB approach, as discussed in Sec. IV, is to construct and solve "unified" governing equations for the momentum and energy. This treatment is made possible because we assume that the solid body is filled with a "virtual" fluid. While the studies that deal with constant density incompressible flows[23] consider the same fluid both inside and outside the body, two-phase investigations[31] choose a "virtual" fluid with highest density and viscosity. However, these studies consider genuinely incompressible flows unlike in the present work where the flow is quasi-incompressible. This raises the pertinent question: how does one choose the properties of the fluid that is assumed to occupy the solid? The strategy to choose the "virtual" fluid is surprisingly simple though and is based on the principle that the fluid flow inside the body must satisfy the incompressibility constraint. This demands that the density within the solid region remain constant at all times so that the overall continuity equation is still satisfied. Consequently,

we choose the "virtual" fluid as a constant density fluid whose density is chosen equal to the initial density of the "real" fluid (at $t = 0$) although any other constant value is also admissible. The thermophysical properties (μ and K) are kept constant and equal to the corresponding values of the "real" fluid which are independent of temperature in the present study. However, if the "real" fluid has variable thermophysical properties, we merely choose to assign their initial values at ($t = 0$) to the "virtual" fluid. One can also appreciate the choice of a constant density for the "virtual" fluid from a physical perspective as well since the incompressible fluid flow is analogous to a rigid solid. We can therefore see that the density of the "virtual" fluid is a free parameter and may be enforced to any realizable constant value within the solid. This was also recognized by Boiron and co-workers,[43] albeit for high Mach number studies. This observation is also true for studies with genuinely incompressible single phase flows[23,27] which however make the most obvious choice for the "virtual" fluid.

D. Computation of P and $\frac{dP}{dt}$ in immersed boundary approach

One of the critical aspects for the low Mach number IB approach is the calculation of thermodynamic pressure and its derivative $\frac{dP}{dt}$. While Eqs. (29) and (30) in Sec. III discuss the computation of these quantities without the IB approach, we now detail its calculations in the framework of the diffuse IB methodology. We see from Eq. (29) that P is computed using the principle of global mass preservation; however, this only applies to the "real" fluid occupying the domain. Subsequently, we compute the spatially invariant thermodynamic pressure as

$$P^{m+1} = \frac{m^o + Ga\sum(1 - \phi_B)_c(\rho\theta)_c^{m+1}\Omega_c}{\sum(1 - \phi_B)_c\Omega_c},$$

(36)

where $\theta_c^{m+1} = \frac{(\rho\theta)_c^{m+1}}{\rho_c^{m+1}}$ is the temperature in the cell and the summation in Eq. (36) is over *all* cells in the domain. However, it is easy to see that cells that lie completely in the solid do not contribute to the calculation of P. It must be remarked that the thermodynamic pressure does not obey the EOS in the solid region. The computation of the temporal derivative $\frac{dP}{dt}$ adopts a similar approach to that for computing P. We know from Eq. (30) that

$$\frac{dP}{dt} = \frac{\gamma}{\Omega_d}C_3 Ga \sum_{e\in(\delta\Omega_d)} \left.\frac{\delta\theta}{\delta n}\right|_e \Delta s_e.$$

(37)

One can cast this in the IB-FV framework using the solid fraction by realizing that Eq. (37) is discrete analog of the following equation:

$$\frac{dP}{dt} = \gamma\frac{C_3 Ga}{\Omega_d} \int_{\Omega_d} \nabla\cdot\nabla\theta\, d\Omega,$$

(38)

where Ω_d is the volume of the domain occupied by the "real" fluid (which is the volume of the entire computational domain minus solid volume) and $\delta\Omega_d$ represents the surface bounding this domain. We therefore have

$$\Omega_d = \sum(1 - \phi_B)_c\Omega_c,$$

(39)

where Ω_c is the volume of a cell and the summation is over all cells in the domain. The volume integral in Eq. (38) which is also over the

region occupied by the "real" fluid can be evaluated in an analogous manner. The integral can be evaluated as the sum of several subintegrals over all nonoverlapping individual cells that contain the "real" fluid in $(1 - \phi_B)$ of their volume. This gives

$$\int_{\Omega_d} \nabla^2 \theta \, d\Omega \approx \sum (1 - \phi_B)_c \int_{\Omega_c} \nabla^2 \theta \, d\Omega,$$

$$\approx \sum \left[(1 - \phi_B)_c \sum_{e \in E(\Omega_c)} \left. \frac{\delta \theta}{\delta n} \right|_e \Delta s_e \right], \qquad (40)$$

where the outer summation in Eq. (40) is over all cells in the computational domain. One can clearly see again that the solid cells do not contribute to the integral and the solid fraction plays a dominant role in the immersed cells to account for the presence of the body in the computation of the temporal derivative of the thermodynamic pressure.

It must be remarked here that $\frac{dP}{dt}$ appears both as a source term in the energy equation as well as the Poisson equation. The latter equation in the IB framework will be dealt with in detail in Sec. IV E, but we remark that $\frac{dP}{dt}$ is necessarily treated in an implicit manner in the energy equation [see Eq. (35)]. This means that the latest available values of temperature are employed and the term is considered as a lagged source term to enable the construction of a system of linear algebraic equations. Subsequently, the linear system for the energy equation is solved several times in each time step—8–10 outer iterations per time step suffice for accurate solutions in the present studies.

E. Unified Poisson equation

The greatest challenge in implementing the diffuse interface IB approach for low Mach flows is arguably the Poisson equation. In the incremental fractional step approach adopted in this work, we solve a Poisson equation for pressure correction. Like with momentum and energy equation, the Poisson equation must also be solved everywhere in the domain, including inside the solid. A close look at the Poisson equation in earlier studies with the diffuse interface IB approach[23,27,31] show that the elliptic partial differential equation (PDE) solved everywhere in the domain is independent of the solid fraction ϕ_B. This is not surprising since these studies considered flows that were incompressible, both inside and outside of the solid. On the contrary, the present work considers the flow to be quasi-incompressible (in general) outside the solid, while it is assumed to remain incompressible inside of it. Therefore, the unified Poisson equation must seamlessly transition from the nonzero divergence constraint applicable in the fluid region to the incompressibility constraint within the solid body. Recall that the "unified" momentum and energy equations transition from the Navier-Stokes equations outside of solid to Dirichlet boundary condition (isothermal wall for θ, no-slip boundary condition for U_f) inside it. The "unified" equations consider that the Dirichlet conditions that strictly apply on the surface may be "extended" into the solid domain. We therefore devise the unified Poisson equation from the understanding that the discrete velocity divergence in any cell may be calculated as

$$(\mathbb{DIV})_c = (1 - \phi_B)_c (\mathbb{DIV})_{(c,f)} + \phi_B (\mathbb{DIV})_{(c,s)}, \qquad (41)$$

where "$\mathbb{DIV}$" is the discrete divergence and the subscripts (c, f) and (c, s) denote the respective expressions for the velocity divergence corresponding to the purely fluid and solid regions. It is easy

to see that $(\mathbb{DIV})_{(c,s)} = 0$ by virtue of incompressibility constraint enforced inside the solid. We therefore have, using Eq. (27),

$$\sum_{e \in E(\Omega_c)} U_e^{m+1} \Delta S_e = \frac{(1 - \phi_B)_c}{P} C_3 Ga$$

$$\times \left[\sum_{e \in E(\Omega_c)} \left. \frac{\delta \theta}{\delta n} \right|_e, -\frac{\Omega_c}{\Omega_d} \sum_{e \in E(\delta \Omega_d)} \left. \frac{\delta \theta}{\delta n} \right|_e \right] \Delta S_e, \qquad (42)$$

which indicates that only the fluid volume must be accounted while handling the quasi-incompressibility constraint on velocity divergence. Following the same approach detailed in Sec. III gives the discrete Poisson equation that reads

$$\frac{2}{3} \Delta t \sum_{e \in E(\Omega_c)} \frac{1}{\rho_e} \left. \frac{\delta \Phi}{\delta n} \right|_e \Delta S_e = \frac{(1 - \phi_B)}{P} C_3 Ga$$

$$\times \left[\sum_{e \in E(\Omega_c)} \left. \frac{\delta \theta}{\delta n} \right|_e - \frac{\Omega_c}{\Omega_d} \sum_{e \in E(\delta \Omega_d)} \left. \frac{\delta \theta}{\delta n} \right|_e \right] \Delta S_e$$

$$- \sum_{e \in E(\Omega_c)} U_e^* \Delta S_e. \qquad (43)$$

It must be mentioned that the quantity $\delta \Omega_d$ in Eqs. (42) and (43) now refers to the bounding surface of the entire computational domain and not just the region containing the "real" fluid, with the presence of the solid surface felt through the $(1 - \phi_B)$ term in these equations. We therefore see that the Poisson equation solved in the IB framework Eq. (43) is evidently dependent on ϕ_B like the momentum and energy equations. This is unlike fully incompressible flows[23] where ϕ_B does not appear in the Poisson equation. Notice that the quantity $\frac{dP}{dt}$ appears as a source term in the Poisson equation but is independent of the hydrodynamic pressure correction that is solved for and the resulting system of linear equations is solved just once in every time step. It must be remarked that the density at the faces is obtained from the centroidal values using the volume-weighted interpolation in this work although one can employ harmonic averaging as well.

The unified Poisson equation becomes completely independent of ϕ_B in the limit as $Ga \to 0$ which is consistent with previous studies,[23,27,31] and this makes the proposed approach generic in nature. It must be noted that while a similar approach was used to tackle a combination of incompressible and compressible flows,[44] the resulting equation for pressure therein is a Helmholtz equation unlike the variable coefficient Poisson equation in the present study. The unified equation presented in this work and the associated IB-FV solver is perhaps the first known instance of an immersed boundary framework for low Mach number quasi-incompressible flow with heat transfer in closed domains.

F. Calculation of density

The calculation of density in each cell in the IB-FV framework is important since it appears in the momentum, energy, and Poisson equations. While the EOS is used to obtain the density in the fluid ("F") cells, its value is maintained constant in all solid ("S") cells. One can therefore write a generic expression for the density in any cell as

$$\rho_c^{m+1} = (1 - \phi_B)_c (P^{m+1} - Ga(\rho \theta)_c^{m+1}) + (\phi_B)_c \rho^0, \qquad (44)$$

where ρ^0 is the constant density enforced within the solid. It must be emphasized that the density is not obtained using the EOS within the solid region which is occupied by a "virtual" fluid.

G. Calculation of Nusselt number

The surface averaged Nusselt number is defined as

$$Nu_{avg} = \frac{1}{C} \int_S Nu \, ds, \qquad (45)$$

where S refers to the surface bounding the solid and C is the area of this surface. For two-dimensional problems considered in this work, C is merely the perimeter of the solid boundary. In the diffuse IB framework, this solid boundary does not conform to the underlying Cartesian mesh and therefore the evaluation of the integral is not trivial. We assume for this purpose that the body may be represented by "stair-step" approximated domain comprising faces shared by the immersed "I" and solid "S" cells. We therefore have

$$Nu_{avg} = \frac{1}{C} \sum Nu_e \Delta S_e, \qquad (46)$$

where summation is over all edges of the stair-step boundary that approximates the solid surface. The local Nusselt number on each edge (or face) may then be estimated as

$$Nu_e = \frac{\theta_I - \theta_S}{\Delta n}, \qquad (47)$$

where θ_I is the value of the temperature in the immersed cell temperature and θ_S is the constant temperature imposed in the solid and Δn is the distance along the face normal direction between the centroids of the "S" and "I" cells sharing the face that constitutes the stair-step approximated domain.

V. NUMERICAL STUDIES

We now consider a collection of test problems involving low Mach number flows with heat transfer to highlight the efficacy of the proposed diffuse interface IB/FV framework. We must assert that there are no well-known test cases involving stationary and moving bodies in the non-Boussinesq regime which makes comparative studies of the proposed solver with the existing literature quite difficult. Nevertheless, for stationary body problems, we make comparison with a previously validated body-fitted finite volume (FV) and for moving geometries validation studies are carried out in the Boussinesq limit. The investigations consider both free and mixed convective flows in enclosures.

A. Natural convection in Boussinesq limit

We consider the natural convection in a square enclosure of side L with a heated cylinder of a diameter $D = 0.2L$ placed at the center. The walls of the enclosure are all kept at the same nondimensional temperature of $\theta_c = -0.5$, while the heated cylinder is maintained at $\theta_h = 0.5$. To simulate the Boussinesq convection, we use $Ga = 0.02$ and studies are carried out for three different Rayleigh numbers, viz., $Ra = 10^4$, $Ra = 10^5$, and $Ra = 10^6$. We have numerically computed the solutions on four different uniform Cartesian meshes with grid resolutions $\Delta x = \Delta y = 0.02$, 0.01, 0.0066, and 0.005 into which cylinder having 200 points is immersed. Following the
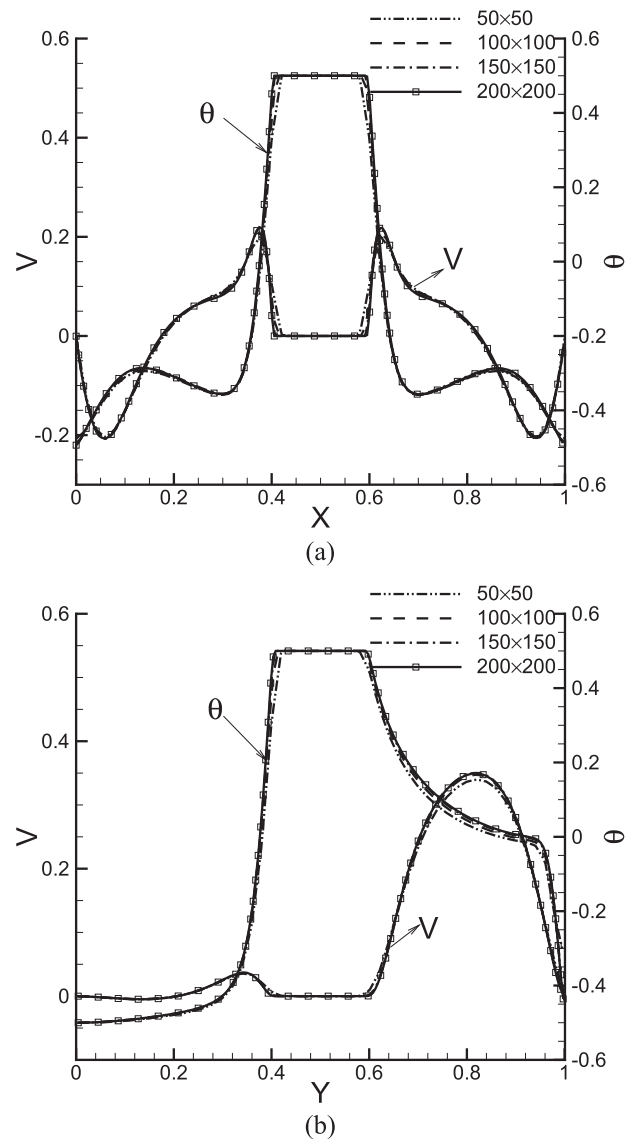

FIG. 5. The centerline velocity and temperature profiles on different Cartesian meshes at $Ga = 0.02$; (a) along the horizontal X-axis and (b) along the vertical Y-axis.

discussion in Sec. IV C, we set the initial density equal to unity inside the solid at all times. The computations employ a constant time step $\Delta t = 0.005$ and converge to steady state. One can see from Fig. 5 that the centerline line velocity and temperature profiles are not very different on the four meshes. However, a comparison of the averaged Nusselt number on the cylinder surface presented in Table II shows that the numerical solutions are grid independent for mesh resolution of $\Delta x = 0.005$. Furthermore, the computed surface Nusselt number for this mesh also agrees well with the results reported in the literature[45,46] for all Rayleigh numbers. This test may therefore be construed both as a primary validation study and a grid independence study. In view of the results obtained for this test case, we

TABLE II. Comparison of the averaged Nusselt number (Nu_{avg}) with other benchmark solutions.

Grid	$Ra = 10^4$	$Ra = 10^5$	$Ra = 10^6$
50 × 50	1.57	2.75	5.02
100 × 100	1.81	3.38	5.88
150 × 150	2.02	3.80	6.10
200 × 200	2.02	3.81	6.11
Shu et al.[45]	2.08	3.78	6.10
Moukalled and Archarya[46]	2.07	3.82	6.10

carry out all computations in the test cases to follow on a 200 × 200 Cartesian mesh.

B. Mixed convection in Boussinesq limit

We now consider the case of mixed convection in the enclosure which is affected by rotating a circular cylinder of $D = 0.4L$ at a constant angular velocity. We choose $Ga = 0.02$, and computations are carried out at two different Richardson numbers, $Ri = 1$ and 10 for a fixed value of $Ra = 10^6$. The cylinder is immersed in a 200 × 200 Cartesian mesh, and the dimensionless angular velocity is equal to 5. It must be remarked that the Reynolds number follows from the chosen value of Ra, Ri, and Pr. The time averaged values of the surface Nusselt number from present studies are compared with the computation of Cui et al.[47] and Liao and Lin[48] in Table III. The depictions of the flow dynamics and temperature distribution in the cavity using streamlines and isotherms are presented in Figs. 6 and 7. It is evident that the flow physics as well as the Nusselt number estimates are in excellent agreement with those reported in the literature. These studies underline the ability of the low Mach IB-FV solver in accurately computing convective flows in the Boussinesq limit and also provide validation of the approach for problems with stationary and moving bodies. We now assess the ability of the solver in computing genuinely non-Boussinesq flows both in free and mixed convection regimes.

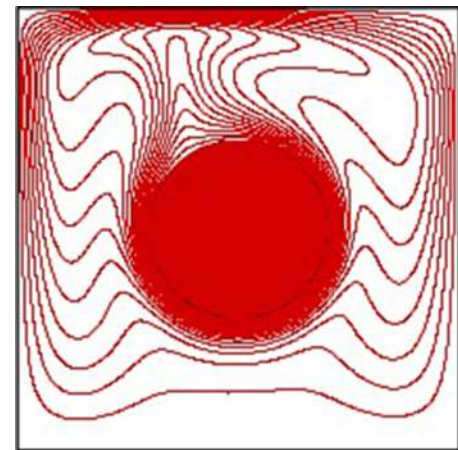## C. Non-Boussinesq natural convection with stationary cylinders

We consider the natural convection in enclosure with non-moving solids at $Ga = 1.2$. This corresponds to large temperature differences between the heated cylinder and cold walls. The dimensionless temperature of the cylinder surface and enclosure

(a)

(b)

FIG. 6. Isotherms (a) present IB-FV and (b) the numerical photograph of Liao and Lin at $Ra = 10^6$. Reproduced with permission from C.-C. Liao and C.-A. Lin, "Mixed convection of a heated rotating cylinder in a square enclosure," Int. J. Heat Mass Transfer **72**, 9–22 (2014). Copyright 2014 Elsevier.

boundary are 0.5 and −0.5, respectively. We reiterate that the thermophysical properties are assumed constant and the square enclosure is discretized by a uniform Cartesian mesh. Numerical investigations are carried out using three different geometric configurations shown in Fig. 8 at $Ra = 10^6$. The triangular and circular cylinder geometries do not conform to the underlying mesh, and the former configuration has sharp corners, all of which are a test of the IB-FV flow solver in addition to the complexities associated with non-Boussinesq convection. A 200 × 200 mesh is employed for these studies except in the triangular cylinder case where the grid used has 250 points in each direction. The steady numerical solutions computed for all three cases are presented using isotherms in Fig. 9 where results corresponding to the Boussinesq regime are also presented. We must remark that there are no reported studies of non-Boussinesq convection with solid bodies in enclosures and therefore adopt the strategy of comparing the results from the
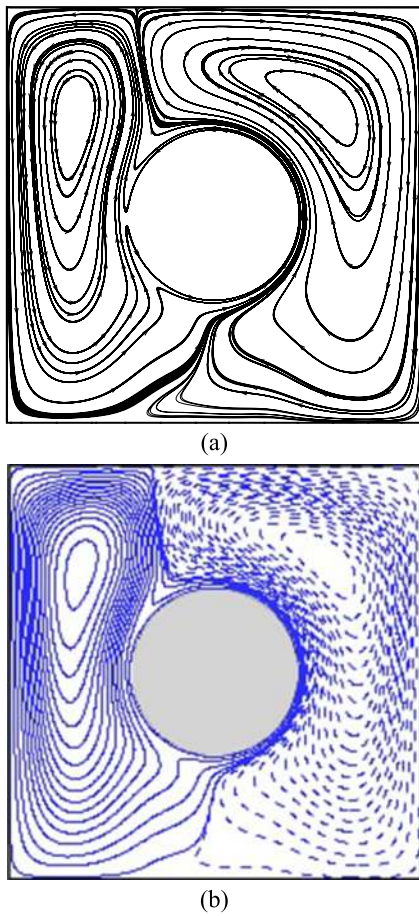
TABLE III. Time averaged Nusselt number ($\overline{Nu}$) on the surface of a circular heated cylinder with other benchmark solutions.

	$Ra = 10^4$		$Ra = 10^5$		$Ra = 10^6$	
	$Ri = 1$	$Ri = 10$	$Ri = 1$	$Ri = 10$	$Ri = 1$	$Ri = 10$
Present	6.25	6.32	6.29	8.97	6.55	15.01
Cui et al.[47]	...	6.40	...	9.01	...	15.18
Liao and Lin[48]	6.41	6.41	6.51	9.0	6.61	15.2

FIG. 7. Streamlines (a) present IB-FV and (b) the numerical photograph of Liao and Lin at $Ra = 10^6$. Reproduced with permission from C.-C. Liao and C.-A. Lin, "Mixed convection of a heated rotating cylinder in a square enclosure," Int. J. Heat Mass Transfer **72**, 9–22 (2014). Copyright 2014 Elsevier.
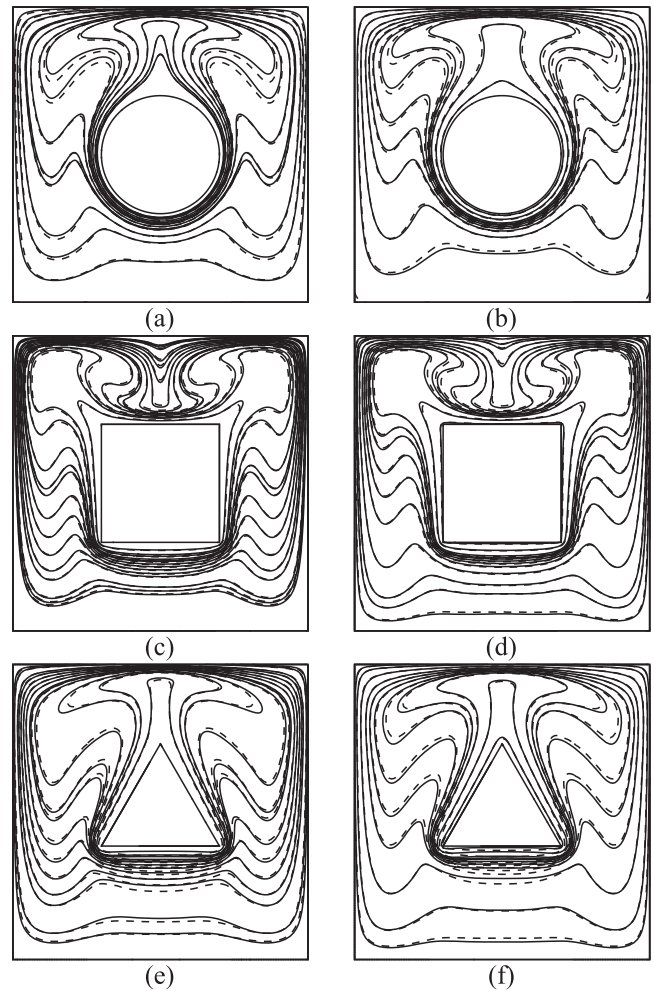

FIG. 9. Isotherms of Boussinesq (left at $Ga = 0.02$) and non-Boussinesq (right at $Ga = 1.2$) flows for different shapes of heated cylinder: [(a) and (b)] circular cylinder, [(c) and (d)] square cylinder, and [(e) and (f)] triangular cylinder. Solid line: IB-FV; dashed line: FV on body-fitted mesh.

IB-FV solver with those obtained using a finite volume solver on unstructured meshes. This flow solver has been previously validated for non-Boussinesq flows[7] although no immersed bodies were considered therein. The unstructured finite volume solver employs triangulated meshes that conform to the cylinder geometry in all three cases. One can see from Fig. 9 that there are no discernible

differences in flow and temperature patterns computed using FV and IB-FV approaches. The centerline temperature and velocity profiles obtained with the immersed boundary approach also agree reasonably well with those computed on unstructured conformal
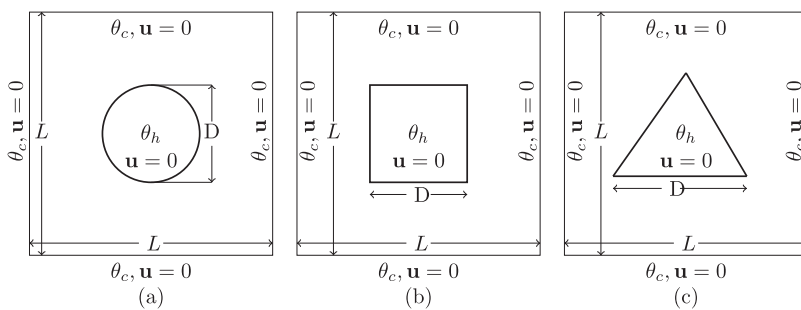

FIG. 8. Schematic diagram of the heated cylinder placed in a square cavity: (a) circular, (b) square, and (c) triangular.
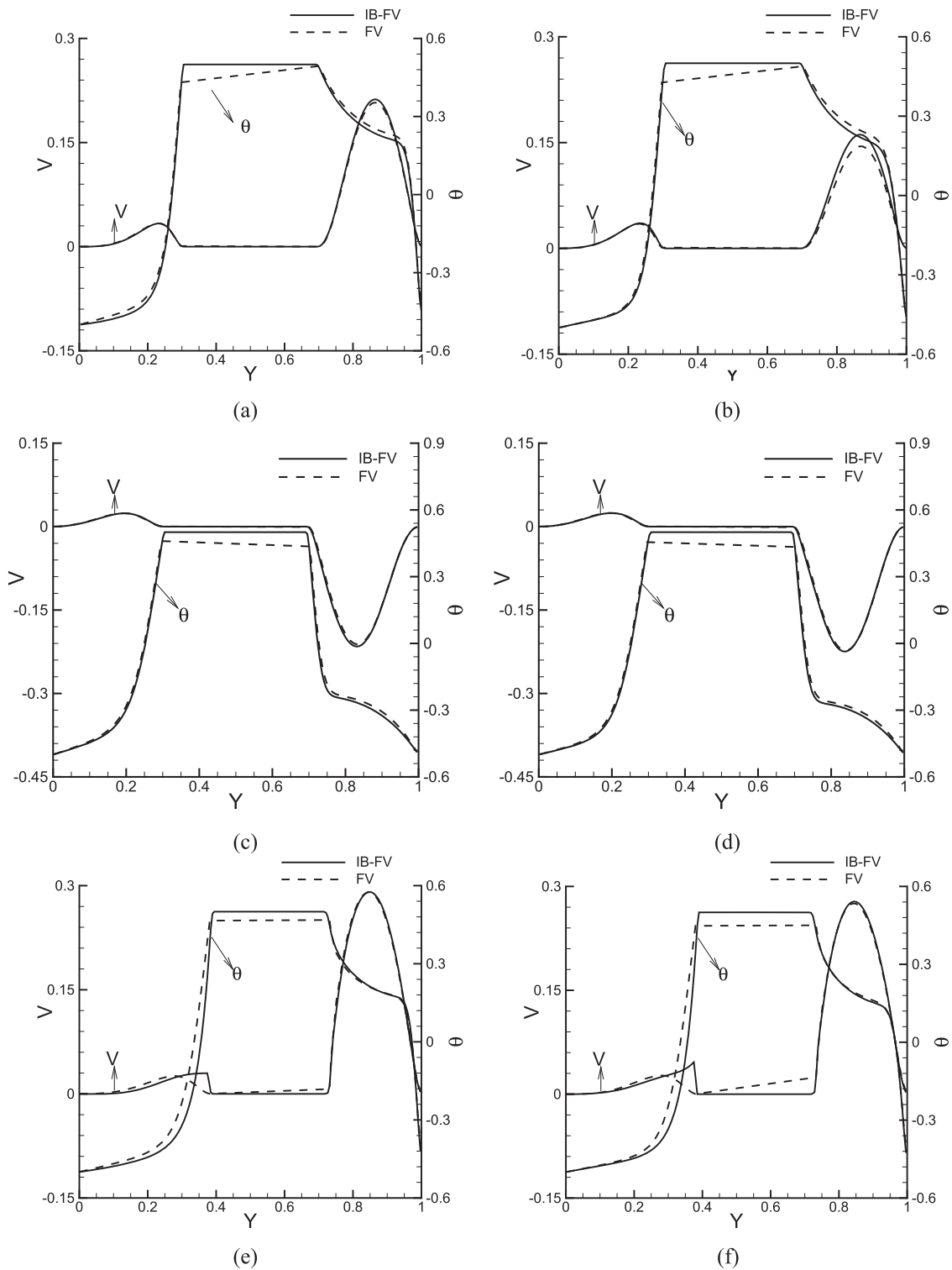
FIG. 10. The centerline velocity and temperature profiles of Boussinesq (left at *Ga* = 0.02) and non-Boussinesq (right at *Ga* = 0.8) flows for different shapes of heated cylinder: [(a) and (b)] circular cylinder, [(c) and (d)] square cylinder, and [(e) and (f)] triangular cylinder.

meshes, as evident from Fig. 10. It can therefore be concluded on the basis of these results that the diffuse-interface immersed boundary approach can compute the flow and thermal fields in the enclosure quite accurately despite some diffusion of the geometric interface including singular corners.

The comparative study of specific interest is the local Nusselt distribution over the cylinder surface. The surface distribution of the dimensionless heat flux is smooth and agrees well with those obtained with body-fitted mesh only in the case of a square cylinder. This may be attributed to the fact that while the Cartesian mesh does not conform to the square cylinder, the geometry is aligned with the grid lines and thus leads to a smooth surface distribution of the Nusselt number, as shown in Figs. 11(c) and 11(d). On the contrary, the variation of the Nusselt number along the surface of
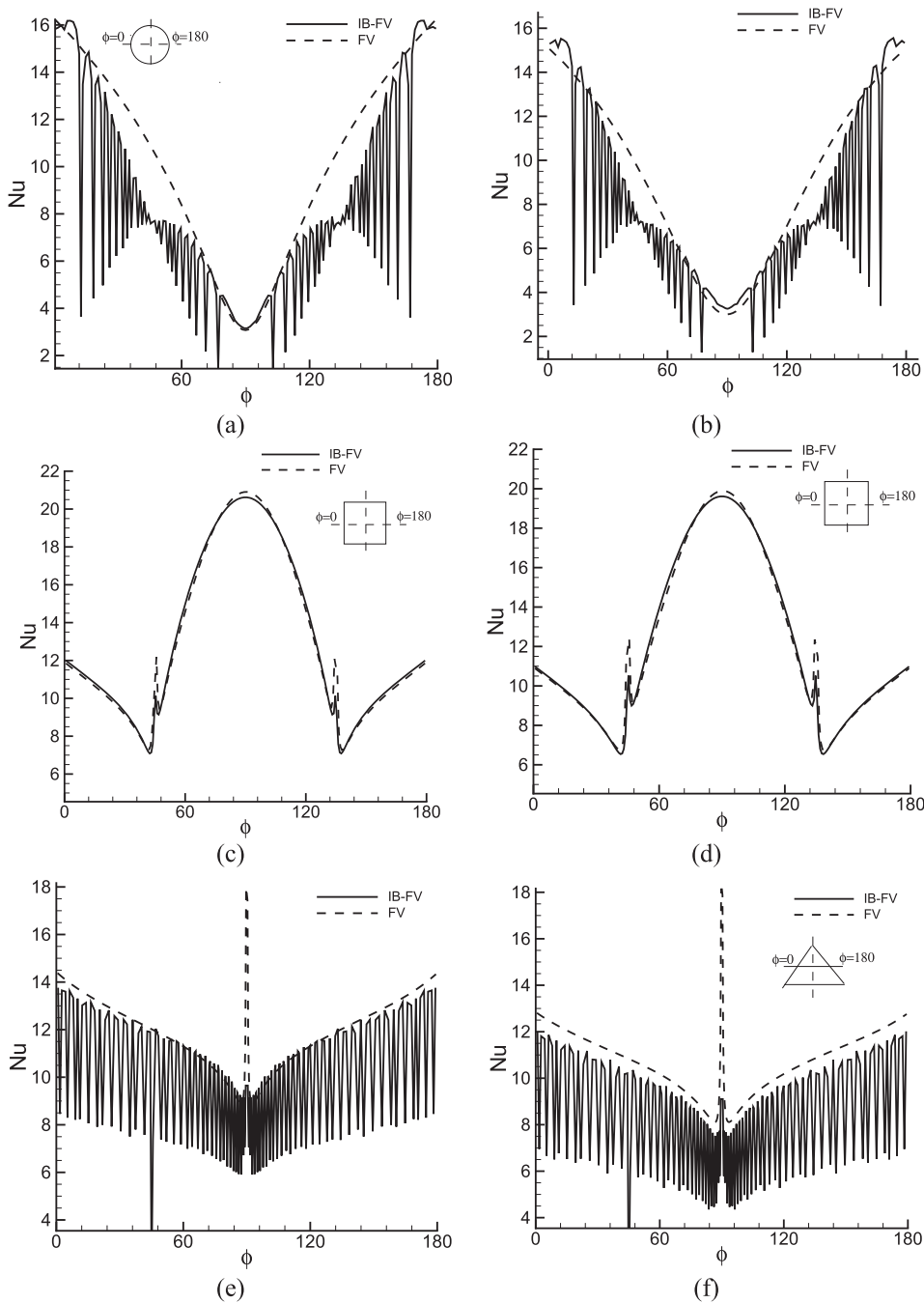

FIG. 11. The comparison of the local Nusselt number distribution for Boussinesq (left at $Ga = 0.02$) and non-Boussinesq (right at $Ga = 0.8$) flows for different shapes of heated cylinder: [(a) and (b)] circular cylinder, [(c) and (d)] square cylinder, and [(e) and (f)] triangular cylinder.

TABLE IV. The averaged Nusselt number (Nu_{avg}) on the surface of different heated cylinders.

	Circular		Square		Triangular	
	$Ga = 0.02$	$Ga = 0.8$	$Ga = 0.02$	$Ga = 0.8$	$Ga = 0.02$	$Ga = 0.8$
IB-FV	17.42	17.01	21.08	20.38	16.94	15.98
FV (conformal mesh)	18.21	17.82	21.12	20.47	17.41	16.43

TABLE V. Time averaged Nusselt number $\overline{Nu}$ on the surface of a triangular heated cylinder at $Ri = 10$.

	$Ra = 10^4$		$Ra = 10^5$		$Ra = 10^6$	
	$Ga = 0.02$	$Ga = 1.2$	$Ga = 0.02$	$Ga = 1.2$	$Ga = 0.02$	$Ga = 1.2$
Present	4.63	5.10	7.12	8.26	11.79	16.65

circular and triangular cylinders, while qualitatively correct, show appreciable high frequency oscillations, as seen in Figs. 11(a), 11(b), 11(e), and 11(f). These spurious oscillations may be attributed to the use of an "approximated domain" approach to calculate local gradient quantities. Importantly, these oscillations persist even in the Boussinesq regime as well and show only a weak dependence on Ga. The local heat flux distribution obtained from the IB-FV
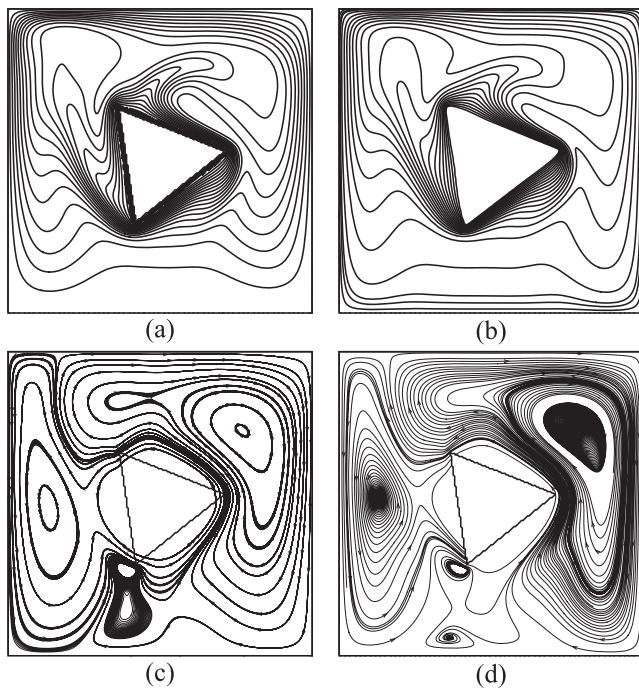

FIG. 12. Isotherms [(a) and (b)] and streamlines [(c) and (d)] for Boussinesq (left at $Ga = 0.02$) and non-Boussinesq (right at $Ga = 1.2$) at $Ra = 10^6$ and $Ri = 10$.
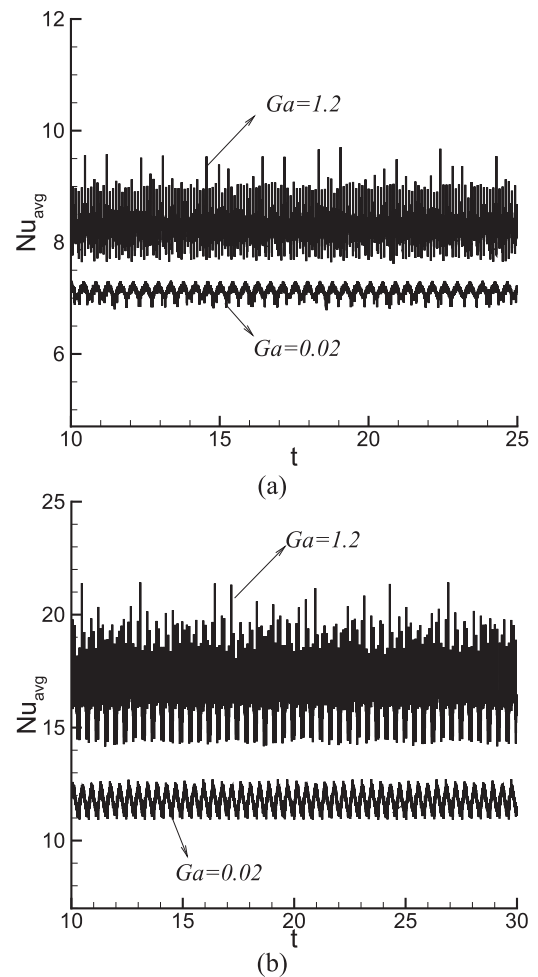

FIG. 13. Temporal history of the surface averaged Nusselt number $\overline{Nu}$ at $Ri = 10$. (a) $Ra = 10^5$, (b) $Ra = 10^6$.
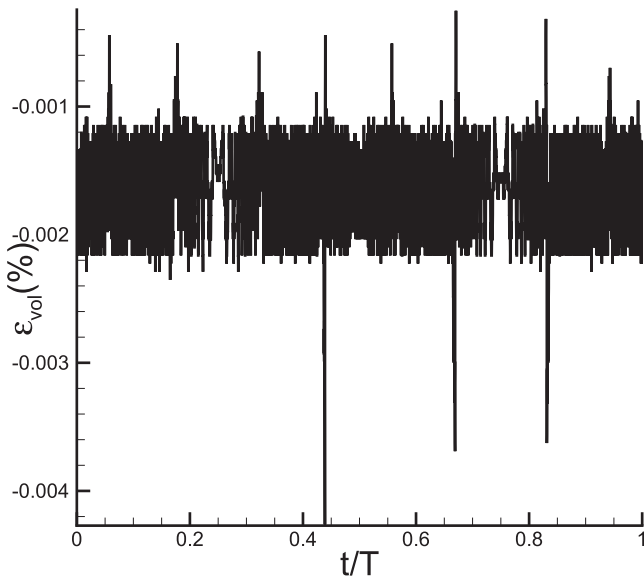
FIG. 14. Temporal history of the volume error for an oscillatory cylinder at $Ra = 10^6$.

boundary into account. Although not shown herein, the Nusselt number distribution and its estimates for the circular and triangular cylinders is expected to improve with further grid refinement although the oscillations appearing in the surface heat flux distribution using the diffuse IB approach are unlikely to diminish on finer meshes.

D. Non-Boussinesq mixed convection: Rotating triangular cylinder

To investigate the capability of the low Mach IB-FV solver for moving body problems, we simulate the flow in a cavity with a heated rotating triangular cylinder. The cylinder of side $D = 0.4L$ kept at $\theta_h = 0.5$ is immersed into the square computational domain whose boundaries are maintained at $\theta_c = -0.5$. The domain is discretized using a 200×200 uniform and a constant dimensionless angular velocity equal to 5 is imposed on the cylinder. Computations are carried out for two different Rayleigh Numbers at $Ga = 1.2$ and $Ri = 10$ with $\Delta t = 0.001$. The time-averaged Nusselt number is shown in Table V for different values of Ga with the estimates using the IB-FV solver on the Cartesian grid. The instantaneous streamlines and isotherms shown in Fig. 12 at $t = 28.2$ indicate that the flow patterns change significantly as Ga increases and this is also reflected in the temporal history of the surface averaged Nusselt number shown in Fig. 13. One can notice that the time histories of the Nusselt number are oscillatory (akin to spurious force oscillations seen in histories of aerodynamic coefficients when computed with a sharp interface IB approach) and a comparison of these histories at the Boussinesq limit with those in a non-Boussinesq regime for the same Ra (see Fig. 13) reveal that the oscillations are higher in the non-Boussinesq regime. These oscillations which now appear in the diffuse IB framework for the mean Nusselt number (which is an integrated quantity) may be referred to as SHOs (spurious heat flux oscillations). It may be noted, however, that their origin is not the fresh cell/dead cell problem that leads to SFOs in sharp interface IB methods and a deeper investigation on mitigating the SHOs is necessary, which is however beyond the scope of the present work.
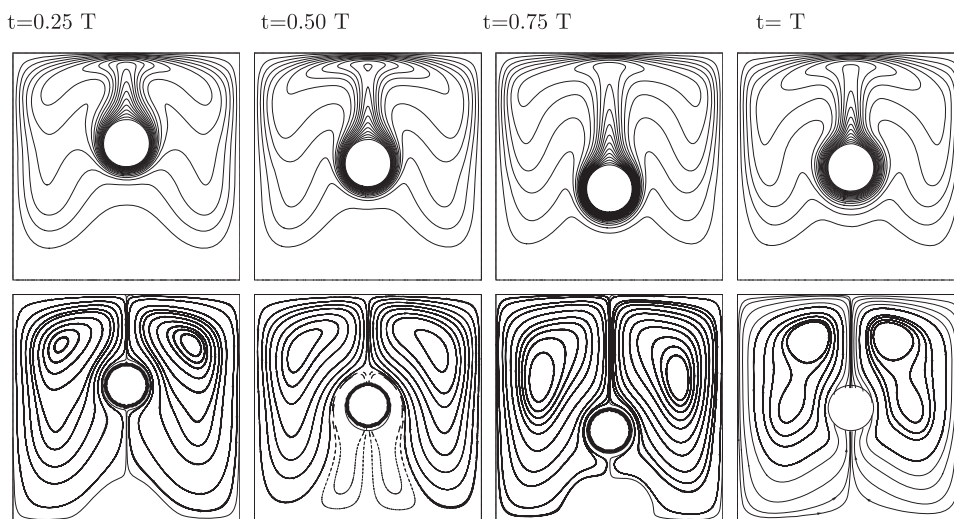
solver has discernible differences from those obtained using the conformal FV solver on unstructured meshes for the case of circular and triangular cylinders. However, the surface-averaged Nusselt number reported in Table IV for the circular and triangular cylinders shows that the estimates using the IB-FV solver on the Cartesian grid, while lesser than those obtained using the unstructured FV solver on the body-fitted mesh, are fairly close to each other. This apparent contradiction can be explained by realizing that for both these geometries, the local Nusselt number distribution is only shown for a part of the boundary (top half of the circular cylinder and slanted edges of the triangular cylinder), while the surface-averaged Nusselt number takes the local heat fluxes over the entire

FIG. 15. Instantaneous isotherms (top) and streamlines (bottom) during a cycle of vertical motion at $Ga = 0.02$ and $Ra = 10^6$.

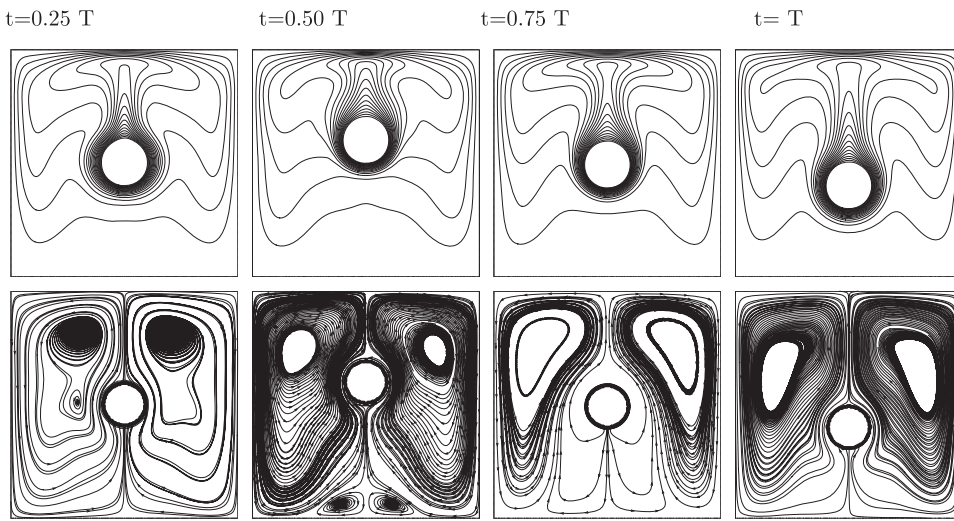| t=0.25 T	t=0.50 T	t=0.75 T	t= T

FIG. 16. Instantaneous isotherms (top) and streamlines (bottom) during a cycle of vertical motion at Ga = 1.2 and Ra = 10^6.

E. Non-Boussinesq mixed convection: Transverse oscillation of circular cylinder

As final test case to assess the utility of the low Mach IB-FV solver, we consider another mixed convection problem in a square enclosure. The details of the computational mesh are the same as those in Sec. V B except that we consider a circular cylinder of diameter $D = 0.2L$ and the motion is oscillatory in the direction parallel to gravity. The transverse motion of the cylinder is described by the dimensionless vertical velocity variation defined by $U = 0.1\cos(1t)$ and calculations are carried out with $\Delta t = 0.001$ at $Ra = 10^6$ both in Boussinesq ($Ga = 0.02$) and non-Boussinesq regimes ($Ga = 1.2$). Figure 14 shows the error in computed cylinder volume which indicates that although the geometric interface is diffused over one cell width, the shape of rigid solid is quite accurately preserved. The isotherms and streamline patterns at four instants during one cycle of oscillation are depicted in Figs. 15 and 16 for both values of Ga. The flow pattern and temperature distributions in the Boussinesq regime agree closely with those computed by Chern et al.[49] (not shown here for brevity) and are clearly different from that obtained for large temperature difference convection although one can identify a left-right symmetry for both velocities and temperature in both Boussinesq and non-Boussinesq regimes. The time-averaged Nusselt number ($\overline{Nu}$) for the Boussinesq regime is tabulated in Table VI and agrees well with the computations of Chern et al.[49] but is smaller than that predicted for the non-Boussinesq regime. It is interesting to note that the temporal histories of the Nusselt number that employ a similar diffuse interface approach[49] for Boussinesq flows show no oscillations, which we believe is a consequence of

smoothing the histories. Similar to the observations for the rotating triangular cylinder in Sec. V D, one can also notice SHOs in the temporal histories for the both regimes shown in Fig. 17. Interestingly, the oscillations are of comparable magnitude for low and high values of Ga for this test case, which point to the fact that the SHOs show weak to moderate dependence on Ga depending on the geometry as well as the imposed motion.

These test problems lend credence to the ability of the novel diffuse interface IB approach to compute low Mach number flows with heat transfer. The numerical investigations clearly highlight that the low Mach IB-FV solver can quite accurately compute the flow dynamics and heat transfer in enclosures with moving geometries at small and large temperature differences although the local Nusselt number distribution and temporal history of the Nusselt
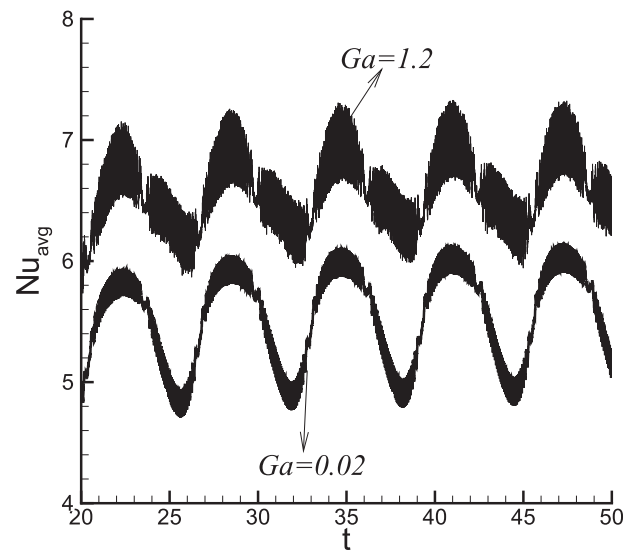
TABLE VI. Comparison of the time averaged Nusselt number $\overline{Nu}$ on the surface of a cylinder with benchmark solution.

	$Ga = 0.02$	$Ga = 1.2$
Present	5.41	6.45
Chern et al.[49]	5.62	. . .

FIG. 17. Temporal history of the averaged Nusselt number at Ra = 10^6.

number are plagued by spurious oscillations. However, the surface and time averaged Nusselt numbers are predicted with reasonable accuracy, with the heat transfer enhanced in the non-Boussinesq regime compared to the Boussinesq regime. Mitigating the SHOs is however important from the numerical standpoint and shall be investigated in a future study.

VI. SUMMARY AND DISCUSSIONS

The diffuse interface IB approach described in the present work extends the philosophy proposed for incompressible flows[23,27] to compute genuinely non-Boussinesq flows with heat transfer. The IB-FV solver may therefore be viewed as a generic approach to solve low Mach number flows with heat transfer. The lack of test problems in the non-Boussinesq regime is an impediment to solver validation which has therefore been carried out largely in the Boussinesq limit. The test problems involving moving solids and high temperature difference free/mixed convection in this work possibly qualify as benchmark cases for validation in the future. The salient features of the proposed IB-FV solver and major findings from the numerical investigations are summarized below.

1. The diffuse interface IB-FV solver for low Mach flows combines the low Mach number formulation for non-Boussinesq flows with the volume-of-solid based immersed boundary technique. In particular, we solve "unified" equations for the conservation laws everywhere that reduce to boundary conditions within the solid and governing equations in the fluid.

2. The proposed IB-FV solver generalizes the philosophy proposed for incompressible flows[23,27] to compute both Boussinesq and non-Boussinesq flows in a unified manner. This generic approach, which is the highlight of the present study, is distinct from previous studies[23,27] for two reasons. First, it accounts for the time dependent thermodynamic pressure and its derivative, with the latter influencing both the energy and Poisson equations. Second, the variable coefficient Poisson equation for hydrodynamic pressure is dependent on the solid fraction unlike earlier studies where only a single pressure is solved for using a Poisson equation devoid of solid fraction. The principle contribution of the methodology detailed in this work is that it recognizes the nature of twin pressures pertinent to low Mach number flows and seamlessly incorporates this aspect into the numerical framework by assuming a constant density incompressible flow inside the rigid solid.

3. The numerical investigations using a low Mach IB-FV solver show that it can reproduce the Boussinesq results at low Ga values. For higher values of Ga, comparisons have been affected with an unstructured FV solver, at least for stationary bodies, which has been validated previously. Studies with rotating and oscillating cylinders at $Ga = 1.2$ reveal differences in the flow dynamics and temperature patterns when compared to the $Ga \rightarrow 0$ limit. These are the first such computations in the non-Boussinesq regime to the best of our knowledge and therefore could become benchmark problems owing to unavailability of test cases for validation.

4. The surface distribution of the local Nusselt number is found to be oscillatory even in steady flows involving stationary complex geometries. In case of unsteady flows with moving bodies,

this reflects as spurious oscillations in the time history of the surface averaged Nusselt number (SHOs). The diffuse interface IB approach fails to obtain relatively smooth distribution of gradient quantities although the mean Nusselt Number (Nu_{avg}) is predicted quite accurately. The time-averaged Nusselt number is greater in the no-Boussinesq regime than in the Boussinesq regime for the same geometry which indicates that the heat transfer is enhanced. One can also observe the spurious oscillations in temporal history in the studies of forced convective flow due to moving cylinders as well.[27] This drawback of the diffuse interface IB approach has not been previously reported and needs to be addressed in the future.

The IB-FV approach for low Mach number flows with heat transfer considers only free and mixed convective flows within enclosures in this work. In open domains, the thermodynamic pressure P is assumed everywhere constant and this simplifies the velocity divergence constraint, the energy equation, and the discrete Poisson equation since $\frac{dP}{dt} = 0$. Such scenarios are typical of reacting flows where the divergence of the velocity field would still be nonzero although it would be independent of the thermodynamic pressure. While the present work does not investigate low Mach flows in open domains, it is evident that the methodology described herein may be applied to tackle such flows with ease. The philosophy of the diffuse interface IB method proposed in this work may also allow the development of such an approach for compressible viscous flows. The development of a diffuse interface IB-FV solver that can compute compressible flows assumes relevance in light of the failure of sharp interface IB approaches to accurately predict heat loads in high Reynolds number hypersonic flows.[33] These recent studies have shown that the use of a "nonconservative" approach of solution reconstruction near boundaries is responsible for under prediction of heat transfer. The idea of evolving a unified treatment for disparate flows in the same domain (incompressible within solid but quasi-incompressible outside of it) may therefore be employed to handle genuinely compressible flows in a quasi-conservative manner, and efforts in this direction are currently underway.

VII. CONCLUSIONS

A novel immersed boundary approach for computing non-Boussinesq flows with rigid solids is proposed in this work. Categorized as a diffuse interface IB approach, the methodology constructs hybrid conservation laws based on the solid volume fraction which are solved everywhere in the domain. This philosophy is combined with a low Mach number formulation in a finite volume framework to devise an immersed boundary finite volume (IB-FV) solver for low Mach number flows with heat transfer. This flow solver has been employed to solve problems in the Boussinesq and genuinely non-Boussinesq regime which involve natural and mixed convection. Numerical investigations considering rotating and oscillating heated cylinders in square enclosures highlight the differences between Boussinesq and non-Boussinesq flows while also underlining the ability of the low Mach IB-FV solver to seamlessly transition across the regimes. The ideas propounded in this work may also be extended to low Mach number reacting flows and compressible viscous flows in future studies.

APPENDIX A: DERIVATION OF EQ. (21)

The nondimensional form of equation of state Eq. (19) can be written as

$$\rho\theta = \frac{P - \rho}{Ga}. \qquad (A1)$$

We substitute Eq. (A1) in the energy equation(18) which gives

$$\frac{\partial}{\partial t}\left(\frac{P - \rho}{Ga}\right) + \nabla \cdot \left(\mathbf{u}\frac{P - \rho}{Ga}\right) = C_3\nabla^2\theta + C_4\left(\frac{dP}{dt}\right). \qquad (A2)$$

Since the thermodynamic pressure remains constant (at any given time instant) everywhere in space, Eq. (A2) simplifies as

$$\frac{1}{Ga}\frac{dP}{dt} - \frac{1}{Ga}\frac{\partial\rho}{\partial t} + \frac{P}{Ga}\nabla \cdot \mathbf{u} - \frac{1}{Ga}\nabla \cdot (\rho\mathbf{u}) = C_3\nabla^2\theta + C_4\left(\frac{dP}{dt}\right). \qquad (A3)$$

Rearranging Eq. (A3) gives

$$\frac{1}{Ga}\left\{\frac{dP}{dt} + P\nabla \cdot \mathbf{u}\right\} - \frac{1}{Ga}\left\{\frac{\partial\rho}{\partial t} + \nabla \cdot (\rho\mathbf{u})\right\} = C_3\nabla^2\theta + C_4\left(\frac{dP}{dt}\right). \qquad (A4)$$

Employing the continuity equation (16) in Eq. (A4) gives

$$\nabla \cdot \mathbf{u} = \frac{1}{P}\left[C_3 Ga\nabla^2\theta - \frac{1}{\gamma}\frac{dP}{dt}\right].$$

This is the expression for velocity divergence given by Eq. (21).

APPENDIX B: DERIVATION OF NORMAL MOMENTUM EQUATION EQ. (23)

The normal momentum equation is obtained by integrating the momentum equation [Eq. (17)] over the finite control volume (see Fig. 1) and projecting along the normal direction to the face. This may be written as

$$\int_\Omega \frac{\partial(\rho\mathbf{u})}{\partial t} \cdot \mathbf{n}_f\, d\Omega + \int_\Omega \nabla \cdot (\rho\mathbf{uu}) \cdot \mathbf{n}_f\, d\Omega$$
$$= -\int_\Omega \nabla p \cdot \mathbf{n}_f\, d\Omega + C_1\int_\Omega \nabla \cdot \left((\nabla\mathbf{u} + \nabla\mathbf{u}^T)\right.$$
$$\left. - \frac{2}{3}(\nabla \cdot \mathbf{u})\mathbf{I}\right) \cdot \mathbf{n}_f\, d\Omega + C_2\int_\Omega (1 - \rho)\hat{\mathbf{e}}_\mathbf{y} \cdot \mathbf{n}_f\, d\Omega. \qquad (B1)$$

We approximate the first term by assuming that ρU_f is an averaged value for the normal momentum (over the control volume Ω) lumped at the face center (see Fig. 1). The volumetric averaging of centroidal values is used for the calculation of face density ρ_f,

$$\int_\Omega \frac{\partial(\rho\mathbf{u})}{\partial t} \cdot \mathbf{n}_f\, d\Omega \approx \frac{d(\rho_f U_f)}{dt}\,\Omega. \qquad (B2)$$

The convective and diffusive fluxes appearing in Eq. (B1) are computed in a manner similar to the collocated grid. The second term

(convective flux) of Eq. (B1) is simplified using Gauss divergence theorem and reads

$$\int_\Omega \nabla \cdot (\rho\mathbf{uu}) \cdot \mathbf{n}_f\, d\Omega = \left[\sum_{e\in E(\Omega)} (\rho_e\mathbf{u}_e U_e)\Delta s_e\right] \cdot \mathbf{n}_f$$
$$= \left[\sum_{e\in E(\Omega)} \begin{pmatrix} \rho_e u_e U_e \\ \rho_e v_e U_e \end{pmatrix}\Delta s_e\right] \cdot (n_{x,f}\ \ n_{y,f}), \qquad (B3)$$

where u_e and v_e represent the components of velocity at the edge center e and U_e denotes normal velocity at the edge e. $n_{x,f}$ and $n_{y,f}$ represent the Cartesian components of outward unit normal vector $\mathbf{n}_f$ at the face "f" (see Fig. 1), and the velocity of Cartesian components at the edge center (u_e, v_e) are obtained from the centroidal velocities using a high-resolution convection scheme. The third term (pressure gradient) can be easily approximated as

$$\int_\Omega \nabla p \cdot \mathbf{n}_f\, d\Omega = \frac{\delta p^m}{\delta n}\Big|_f\,\Omega. \qquad (B4)$$

The fourth term (diffusive flux) of Eq. (B1) is simplified using Gauss divergence theorem and reads

$$C_1\int_\Omega \nabla \cdot \left((\nabla\mathbf{u} + \nabla\mathbf{u}^T) - \frac{2}{3}(\nabla \cdot \mathbf{u})\mathbf{I}\right) \cdot \mathbf{n}_f\, d\Omega$$
$$= C_1\left[\sum_{e\in E(\Omega)} ((\nabla\mathbf{u}_e + \nabla\mathbf{u}_e^T - \frac{2}{3}(\nabla \cdot \mathbf{u})\mathbf{I}) \cdot \mathbf{n}_e)\Delta s_e\right] \cdot \mathbf{n}_f$$
$$= C_1\left[\sum_{e\in E(\Omega)} \begin{pmatrix} \tau_{xx}\big|_e n_{x,e} + \tau_{xy}\big|_e n_{y,e} \\ \tau_{yx}\big|_e n_{x,e} + \tau_{yy}\big|_e n_{y,e} \end{pmatrix}\Delta s_e\right] \cdot (n_{x,f}\ \ n_{y,f}), \qquad (B5)$$

where $n_{x,e}$ and $n_{y,e}$ represent the Cartesian components of outward unit normal vector $\mathbf{n}_e$ and components of the deviatoric stress tensor at the edge "e" reads

$$\tau_{xx}\big|_e = 2\frac{\delta u}{\delta x}\Big|_e - \frac{2}{3}\left(\frac{\delta u}{\delta x}\Big|_e + \frac{\delta v}{\delta y}\Big|_e\right), \quad \tau_{xy}\big|_e = \left(\frac{\delta u}{\delta y}\Big|_e + \frac{\delta v}{\delta x}\Big|_e\right),$$
$$\tau_{yx}\big|_e = \left(\frac{\delta u}{\delta y}\Big|_e + \frac{\delta v}{\delta x}\Big|_e\right), \quad \tau_{yy}\big|_e = 2\frac{\delta v}{\delta y}\Big|_e - \frac{2}{3}\left(\frac{\delta u}{\delta x}\big|_e + \frac{\delta v}{\delta y}\Big|_e\right).$$

The last term of Eq. (B1) may be simplified as

$$C_2\int_\Omega (1 - \rho)\hat{\mathbf{e}}_\mathbf{y} \cdot \mathbf{n}_f\, d\Omega = C_2(1 - \rho_f^m)n_{y,f}\,\Omega. \qquad (B6)$$

Combining the discrete expressions from Eqs. (B2)–(B6), we obtain the discrete normal momentum equation Eq. (23).

APPENDIX C: ORDER OF ACCURACY

We study the order of accuracy of the IB-FV solver by using a manufactured solution to the Navier-Stokes equations. The analytical solution given below satisfies the mass, momentum, and energy equations for a constant density and constant viscosity incompressible flow

$$u = -\cos(2\pi x)\sin(2\pi y)e^{\frac{-8\pi^2 t}{Re}}, \tag{C1}$$

$$v = \sin(2\pi x)\cos(2\pi y)e^{\frac{-8\pi^2 t}{Re}}, \tag{C2}$$

$$p = \frac{-(\cos(4\pi x) + \cos(4\pi y))}{4}e^{\frac{-16\pi^2 t}{Re}}, \tag{C3}$$

$$\theta = (\cos(4\pi x) + \cos(4\pi y))e^{\frac{-8\pi^2 t}{RePr}}. \tag{C4}$$

We consider a 0.5×0.5 domain into which a circular cylinder of diameter 0.2 is centrally immersed. For the purpose of study, we do not consider the cylinder as a solid but rather as a region where the exact solution given by Eqs. (C1)–(C4) is prescribed at all times. The numerical solution is computed in all cells outside of the cylinder (including those cut by it) using the IB-FV solver. Since the analytical solution is known, it is possible to compute the discretization error both in space and time. For studies of spatial discretization error, we consider four progressively refined meshes starting from a 40×40 grid with constant $\Delta t = 0.001$. The temporal discretization error is computed by carrying out simulations on the finest mesh resolutions $\Delta x = 0.003\,128$ at four different time steps ($\Delta t = 0.01, 0.005, 0.0025, 0.001\,25$). The simulations are carried at up to $t = 0.1$ at $Re = 100$ and $Pr = 0.7$ in all cases. Figures 18 and 19 show the variation of L_∞ norm of error with spatial and temporal step sizes, respectively. The error is computed as the difference between the exact solution and the numerical solution in each cell. It is easy to see that the solver preserves the expected second-order accuracy both in space and time even when the interface is treated using the IB approach. This study proves that the IB-FV solver is nominally second-order accurate both in space and time, which suffice for most problems in fluid flow and heat transfer.
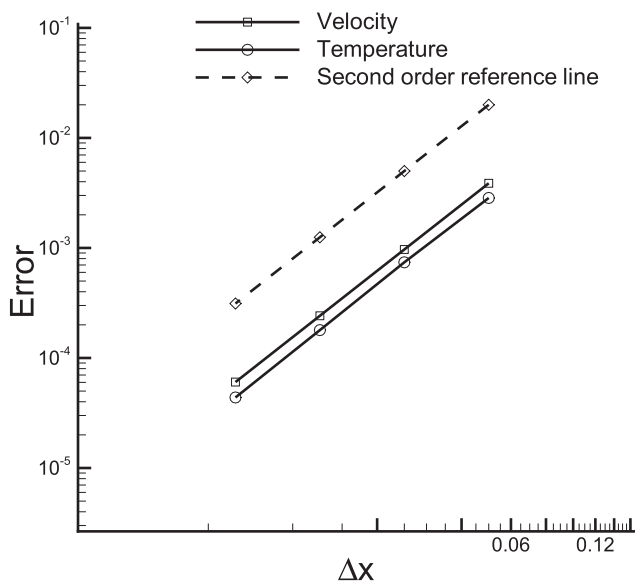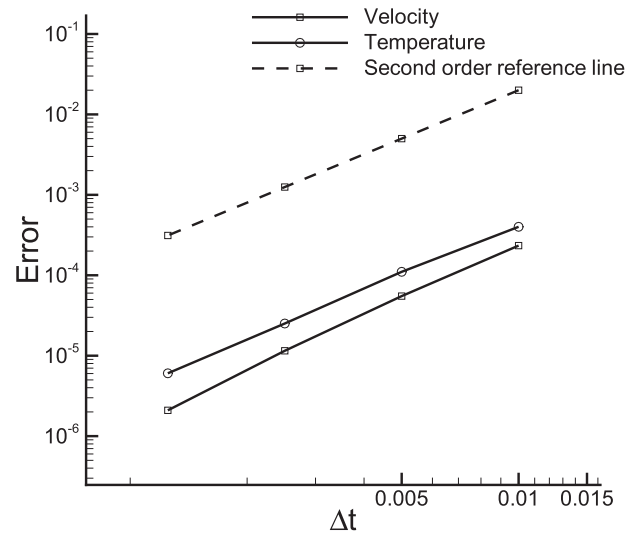

FIG. 18. Spatial accuracy study.

FIG. 19. Temporal accuracy study.

REFERENCES

[1] G. D. V. Davis, "Natural convection of air in a square cavity: A bench mark numerical solution," Int. J. Numer. Methods Fluids **3**, 249–264 (1983).

[2] N. C. Markatos and K. A. Pericleous, "Laminar and turbulent natural convection in an enclosed cavity," Int. J. Heat Mass Transfer **27**, 755–772 (1984).

[3] M. Usman, T. Zubair, M. Hamid, R. U. Haq, and W. Wang, "Wavelets solution of MHD 3-D fluid flow in the presence of slip and thermal radiation effects," Phys. Fluids **30**, 023104 (2018).

[4] M. Usman, M. Hamid, T. Zubair, R. U. Haq, and W. Wang, "Cu-Al$_2$O$_3$/water hybrid nanofluid through a permeable surface in the presence of nonlinear radiation and variable thermal conductivity via LSM," Int. J. Heat Mass Transfer **126**, 1347–1356 (2018).

[5] M. Hamid, M. Usman, T. Zubair, R. U. Haq, and W. Wang, "Shape effects of MoS$_2$ nanoparticles on rotating flow of nanofluid along a stretching surface with variable thermal conductivity: A Galerkin approach," Int. J. Heat Mass Transfer **124**, 706–714 (2018).

[6] M. Usman, F. A. Soomro, R. U. Haq, W. Wang, and O. Defterli, "Thermal and velocity slip effects on Casson nanofluid flow over an inclined permeable stretching cylinder via collocation method," Int. J. Heat Mass Transfer **122**, 1255–1263 (2018).

[7] M. Kumar and G. Natarajan, "On the role of discrete mass conservation for non-Boussinesq flow simulations in enclosures," Int. J. Heat Mass Transfer **104**, 1283–1299 (2017).

[8] O. Bouloumou, E. Serre, P. Bontoux, and J. Fröhlich, "A 3D pseudo-spectral low mach-number solver for buoyancy driven flows with large temperature differences," Comput. Fluids **66**, 107–120 (2012).

[9] M. Kumar and G. Natarajan, "Unified solver for thermobuoyant flows on unstructured meshes," in *Fluid Mechanics and Fluid Power—Contemporary Research*, edited by A. K. Saha, D. Das, R. Srivastava, P. K. Panigrahi, and K. Muralidhar (Springer India, 2017), pp. 569–580.

[10] P. L. Quéré, R. Masson, and P. Perrot, "A Chebyshev collocation algorithm for 2D non-boussinesq convection," J. Comput. Phys. **103**, 320–335 (1992).

[11] J. Vierendeels, B. Merci, and E. Dick, "A multigrid method for natural convective heat transfer with large temperature differences," J. Comput. Appl. Math. **168**, 509–517 (2004).

[12] P. L. Quéré, C. Weisman, J. Vierendeels, E. Dick, M. Braack, F. Dabbene, A. Beccantini, E. Studer, T. Kloczko, C. Corre, V. Heuveline, M. Darbandi, and S. F. Hosseinizadeh, "Modelling of natural convection flows with large temperature differences: A benchmark problem for low mach number solvers

part 2 reference solutions," ESAIM: Math. Modell. Numer. Anal. **39**, 617–621 (2005).

[13] M. Parmananda, A. Dalal, and G. Natarajan, "Unified framework for buoyancy induced radiative-convective flow and heat transfer on hybrid unstructured meshes," Int. J. Heat Mass Transfer **126**, 908–925 (2018).

[14] M. Parmananda, R. Thirumalaisamy, A. Dalal, and G. Natarajan, "Investigations of turbulence-radiation interaction in non-Oberbeck-Boussinesq buoyancy-driven flows," Int. J. Therm. Sci. **134**, 298–316 (2018).

[15] J. Bell, "AMR for low Mach number reacting flows," in Proceedings of the Chicago Workshop on Adaptive Mesh Refinement Methods, Chicago, 2003, LBNL Report LBNL-54351.

[16] D. Coakley, P. Raftery, and M. Keane, "A review of methods to match building energy simulation models to measured data," Renewable Sustainable Energy Rev. **37**, 123–141 (2014).

[17] R. Mittal and G. Iaccarino, "Immersed boundary methods," Annu. Rev. Fluid Mech. **37**, 239–261 (2005).

[18] Y.-H. Tseng and J. H. Ferziger, "A ghost-cell immersed boundary method for flow in complex geometry," J. Comput. Phys. **192**, 593–623 (2003).

[19] S. Sangmook, B. S. Yong, K. I. Chul, K. Y. Jig, and G. J. Sam, "Computations of flow over a flexible plate using the hybrid Cartesian/immersed boundary method," Int. J. Numer. Methods Fluids **55**, 263–282 (2007).

[20] R. Glowinski, T. Pan, T. Hesla, D. Joseph, and J. Périaux, "A fictitious domain approach to the direct numerical simulation of incompressible viscous flow past moving rigid bodies: Application to particulate flow," J. Comput. Phys. **169**, 363–426 (2001).

[21] Q. Liu and O. V. Vasilyev, "A Brinkman penalization method for compressible flows in complex geometries," J. Comput. Phys. **227**, 946–966 (2007).

[22] B. Kadoch, D. Kolomenskiy, P. Angot, and K. Schneider, "A volume penalization method for incompressible flows and scalar advection–diffusion with moving obstacles," J. Comput. Phys. **231**, 4365–4383 (2012).

[23] D. Pan, "An immersed boundary method for incompressible flows using volume of body function," Int. J. Numer. Methods Fluids **50**, 733–750 (2006).

[24] Y. Wang, C. Shu, and L. M. Yang, "Boundary condition-enforced immersed boundary-lattice Boltzmann flux solver for thermal flows with Neumann boundary conditions," J. Comput. Phys. **306**, 237–252 (2016).

[25] W. Ren, C. Shu, and W. Yang, "An efficient immersed boundary method for thermal flow problems with heat flux boundary conditions," Int. J. Heat Mass Transfer **64**, 694–705 (2013).

[26] Y. Hu, D. Li, S. Shu, and X. Niu, "Study of multiple steady solutions for the 2D natural convection in a concentric horizontal annulus with a constant heat flux wall using immersed boundary-lattice Boltzmann method," Int. J. Heat Mass Transfer **81**, 591–601 (2015).

[27] A. K. De, "A diffuse interface immersed boundary method for convective heat and fluid flow," Int. J. Heat Mass Transfer **92**, 957–969 (2016).

[28] J. H. Seo and R. Mittal, "A high-order immersed boundary method for acoustic wave scattering and low-Mach number flow-induced sound in complex geometries," J. Comput. Phys. **230**, 1000–1019 (2011).

[29] A. Abdelsamie, G. Fru, T. Oster, F. Dietzsch, G. Janiga, and D. Thévenin, "Towards direct numerical simulations of low-Mach number turbulent reacting and two-phase flows using immersed boundaries," Comput. Fluids **131**, 123–141 (2016).

[30] L. Zhang, K. Liu, and C. You, "Fictitious domain method for fully resolved reacting gas–solid flow simulation," J. Comput. Phys. **299**, 215–228 (2015).

[31] J. K. Patel and G. Natarajan, "Diffuse interface immersed boundary method for multi-fluid flows with arbitrarily moving rigid bodies," J. Comput. Phys. **360**, 202–228 (2018).

[32] H. Udaykumar, R. Mittal, P. Rampunggoon, and A. Khanna, "A sharp interface Cartesian grid method for simulating flows with complex moving boundaries," J. Comput. Phys. **174**, 345–380 (2001).

[33] S. Brahmachary, private communication (2018).

[34] P. K. Kundu, I. M. Cohen, and D. R. Dowling, *Fluid Mechanics* (Elsevier Science, 2012).

[35] S. Paolucci, *Filtering of Sound from the Navier-Stokes Equations* (Sandia National Laboratories Livermore, CA, USA, 1982).

[36] G. Natarajan and F. Sotiropoulos, "IDeC(k): A new velocity reconstruction algorithm on arbitrarily polygonal staggered meshes," J. Comput. Phys. **230**, 6583–6604 (2011).

[37] G. Natarajan and F. Sotiropoulos, "Adaptive finite volume incompressible Navier-Stokes solver for 3D flows with complex immersed boundaries," in Proceedings of the 62nd APS-DFD Annual Meeting, Minneapolis, MN, 2009.

[38] M. Basumatary, G. Natarajan, and S. C. Mishra, "Defect correction based velocity reconstruction for physically consistent simulations of non-Newtonian flows on unstructured grids," J. Comput. Phys. **272**, 227–244 (2014).

[39] See http://www.mcs.anl.gov/petsc/ for Petsc webpage; accessed November 2018.

[40] See http://www.ssisc.org/lis/ for Lis webpage; accessed November 2018.

[41] I. Borazjani, L. Ge, and F. Sotiropoulos, "Curvilinear immersed boundary method for simulating fluid structure interaction with complex 3D rigid bodies," J. Comput. Phys. **227**, 7587–7620 (2008).

[42] M. Kumar and G. Natarajan, "A diffuse interface immersed boundary framework for conjugate heat transfer problems," Phys. Rev. E **99**, 053304 (2019).

[43] O. Boiron, G. Chiavassa, and R. Donat, "A high-resolution penalization method for large mach number flows in the presence of obstacles," Comput. Fluids **38**, 703–714 (2009).

[44] V. Daru, P. L. Quéré, M.-C. Duluc, and O. L. Maître, "A numerical method for the simulation of low Mach number liquid–gas flows," J. Comput. Phys. **229**, 8844–8867 (2010).

[45] C. Shu, H. Xue, and Y. D. Zhu, "Numerical study of natural convection in an eccentric annulus between a square outer cylinder and a circular inner cylinder using DQ method," Int. J. Heat Mass Transfer **44**, 3321–3333 (2001).

[46] F. Moukalled and S. Acharya, "Natural convection in the annulus between concentric horizontal circular and square cylinders," J. Thermophys. Heat Transfer **10**, 524–531 (1996).

[47] X. Cui, X. Yao, Z. Wang, and M. Liu, "A coupled volume penalization-thermal lattice Boltzmann method for thermal flows," Int. J. Heat Mass Transfer **127**, 253–266 (2018).

[48] C.-C. Liao and C.-A. Lin, "Mixed convection of a heated rotating cylinder in a square enclosure," Int. J. Heat Mass Transfer **72**, 9–22 (2014).

[49] M.-J. Chern, D. Z. Noor, C.-B. Liao, and T.-L. Horng, "Direct-forcing immersed boundary method for mixed heat transfer," Commun. Comput. Phys. **18**, 1072–1094 (2015).